行政院國家科學委員會專題研究計畫成果報告

※※※※※※※※※※※※※※※※※※※※※※※※※※※※※※※※※※

氣態分子之動力學、光分解反應、與動態行為研究、及雷射光譜儀在分析化學之應用（3/3）

※※※※※※※※※※※※※※※※※※※※※※※※※※※※※※※※※※

計畫類別： 特約研究計畫

計畫編號： NSC 88-2113-M-002-010

執行期間：87 年 8 月 1 日至 88 年 7 月 31 日

個別型計畫：計畫主持人：林金全
共同主持人：

整合型計畫：總計畫主持人：
子計畫主持人：

註：整合型計畫組報告與子計畫成果報告請分開編印各成一冊，彙整一起繳送國科會。

處理方式：☑可立即對外提供參考
（請打Ｖ）□一年後可對外提供參考
□兩年後可對外提供參考
（必要時，本會得展延發表時限）

執行單位： 國立台灣大學化學系

中華民國 89 年 3 月 24 日

關鍵字：反應動力學；雷射誘發螢光；光分解

我們自 85.8.1-88.7.31 執行國科會專題計畫，氣態分子之動力學、光分解反應、與動態行為研究、及雷射光譜儀在分析化學之應用。在第三年（87 年）中已完成的結果有：

1. Y. R. Ou, D. K. Liu, and K.C. Lin "Ab initio calculation for potential energy surfaces relevant to the microscopic reaction pathways for $Mg(3s3p\,^1P_1)+H2 \rightarrow MgH(^2\Sigma^+)+H$", J. Chem. Phys, 108 (4), 1475(1998).

2.C. F. Nien, and K. C. Lin "Kinetic investigation of the quenching of $Mg(3s3p\,^1P_1)$atoms in collisions with CH_4 over the temperature range from 660 to 850 K", American Institute of Physics, 109, 18, 7821(1998).

3.C. B. Ke, and K. C. Lin "Spatially Resolved Temperature determination of an Air/Actylene Flame Using the Two-Step laser-Enchanced Ionization Technique", Applied Spectroscopy, 52, 2, 187(1998).

Keyword :

reaction dynamics ; laser-induced fluorescence ;photodissociation

We have accomplished the third-year task (contract no.NSC88-2113-M-002-010) of a three-year term project. The results lead to serveral papers published. They are listed as follow :

1. Y. R. Ou, D. K. Liu, and K.C. Lin "Ab initio calculation for potential energy surfaces relevant to the microscopic reaction pathways for $Mg(3s3p^1P_1)+H2 \rightarrow MgH(^2\Sigma^+)+H$", J. Chem. Phys, 108 (4), 1475(1998).

2.C. F. Nien, and K. C. Lin "Kinetic investigation of the quenching of $Mg(3s3p^1P_1)$atoms in collisions with CH_4 over the temperature range from 660 to 850 K", American Institute of Physics, 109, 18, 7821(1998).

3.C. B. Ke, and K. C. Lin "Spatially Resolved Temperature determination of an Air/Actylene Flame Using the Two-Step laser-Enchanced Ionization Technique", Applied Spectroscopy, 52, 2, 187(1998).

Kinetic investigation of the quenching of $Mg(3s3p\ ^1P_1)$ atoms in collisions with CH_4 over the temperature range from 660 to 850 K

Chia-Fu Nien and King-Chuen Lin[a)]
Department of Chemistry, National Taiwan University, Taipei, and Institute of Atomic and Molecular Sciences, Academia Sinica, Taipei, Taiwan 106, Republic of China

(Received 10 March 1998; accepted 4 August 1998)

Temperature dependence of the quenching efficiency of $Mg(3s3p\ ^1P_1)$ by CH_4 collision in the Ar bath gas has been studied over the temperature range of 660–850 K, using a pump–probe technique with time-resolved laser-induced fluorescence (LIF) as detection. The obtained thermal rate coefficients are attributed to physical and chemical quenching. The former contribution is evaluated to be less than 6.7×10^{-11} cm^3 molecule^{-1} s^{-1}, while the latter one is $(0.59-1.12)\times10^{-11}\exp(5.75-6.54\ \text{kcal mol}^{-1}/RT)$ cm^3 molecule^{-1} s^{-1} (R is gas constant; T is temperature). The chemical reaction dominates over the exit channels, especially in the low temperature. The negative temperature dependence indicates the existence of a depth-well intermediate. The observed depth-well energy below the reactants is about twice as small as that evaluated theoretically. This bound state is anticipated to locate in the region of surface crossing between the excited and the ground states. We adopted several models to account for the kinetic data as a function of temperature. The orbiting and absorbing-sphere models cannot be validly applied to the current system. The angle-dependent line of normals (ADLN) model takes into account the angular dependence of the threshold energy. The ADLN fit to the measured kinetic data is consistent with the insertion mechanism reported previously, which shows energetic preference to the end-on attack. © *1998 American Institute of Physics.* [S0021-9606(98)00942-8]

I. INTRODUCTION

The way to cleave alkyl C–H bonds in the hydrocarbons by metal atoms has been an attractive subject in reaction dynamics, not only due to fundamental interest but also for the practical application in catalysis. Methane is the smallest, but stable, hydrocarbon. Methane, like H_2, has been identified as an inefficient quencher toward the excited alkali-metal atoms; its lowest unoccupied molecular orbital is the antibonding σ^* orbital.[1,2] However, it differs in reactivity when the metal–atom excitation energy exceeds the required exothermic threshold. For instance, studies have revealed that the mixture of highly excited K-atom vapor and H_2 may yield the KH product. When the mixture is replaced by CH_4 no significant chemical reaction is observed, although the bond strength of C–H in methane is weaker than that of H–H.[3,4] On the other hand, both H_2 and CH_4 may feasibly react with the Mg $3s3p\ ^1P_1$ atom to yield MgH.[5–14] In this sense, to study the reaction of $Mg(3s3p\ ^1P_1)$ with CH_4 is chemically interesting.

In the early 1980s Breckenridge and co-workers investigated the reactions of $Mg(3\ ^1P_1)$ with a series of alkane and alkene hydrocarbons.[6,7] In the reactions, MgH rotational populations had presented a bimodal distribution, in which the deconvoluted low rotational components were almost identical. Thus, it was suggested that a nearly linear Mg–H–C configuration might be the predominant mechanism, since the bond rupture in this manner was least affected by the local molecular environment. Nevertheless, in subsequent studies, they also noted that other reaction pathways including Mg insertion into the C–H bond of the polyatomic reactant should not be ruled out.[14,15] In a recent study on $Mg(3\ ^1P_1)+CH_4$ reaction dynamics, Kleiber and co-workers affirmed the dominance of the Mg insertion mechanism by using a far-wing scattering technique.[10] The MgH low-N and high-N distributions were measured to originate from the same mechanism controlled by the exit channel branching, but independent of how and where the $MgCH_4$ complex was excited in the entrance channel. In our measurement of temperature dependence, the shapes of bimodal rotational distributions were found to be the same within the experimental error.[13] The conclusion also supported the insertion mechanism. According to *ab initio* potential surface calculation by Chaquin *et al.*,[16] a substantial potential barrier of 35 kcal mol^{-1} may be encountered as $Mg(3\ ^1P_1)$ approaches CH_4 along a collinear Mg–H–C axis. In contrast, the insertion pathway may suffer the lowest energy barrier—$<$6.9 kcal mol^{-1}. Considering the reported geometry of the transition state, Breckenridge further suggested that the most favorable mode of C–H bond side-on attack should be highly asymmetric and H atom centered.[14] $Mg(p\pi)-CH(\sigma^*)$ overlap occurs closer to the H atom to avoid repulsion from the other C–H bonds. In view of these studies, the $Mg(3\ ^1P_1)$ plus CH_4 reaction favors a Mg-insertion mechanism, irrespective of the geometry of the entrance approach.

In contrast to the understanding of reaction dynamics, information on the kinetic data of the $Mg(3\ ^1P_1)$ with CH_4 collision appears to be insufficient. Thus far, Breckenridge

a)Author to whom correspondence should be addressed; electronic mail: kclin@hp9k720.iams.sinica.edu.tw

and co-workers have made the major contribution.[15] Early in the 1980s the authors studied the total deactivation cross sections of $Mg(3\,^1P_1)$ by various small molecules and demonstrated that their quenching behaviors were controlled by entrance channel, in accord with the prediction of long-range attractive interaction. Methane was the only exception in their studies of hydrocarbons, showing a quenching cross section lower than expected from the C_6 correlation. Since the C–H bond strength is greater than 100 kcal/mol of the $Mg(3\,^1P_1)$ electronic energy, they have suggested that the insertion of $Mg(3\,^1P_1)$ into the C–H bond with a slight chemical barrier may account for the discrepancy from the behavior expected by long-range interaction. The *ab initio* potential barrier for the insertion approach was evaluated by Chaquin *et al.* to be less than 6.9 kcal/mol.[16] The insertion mechanism was energetically favored. The MgH was considered as the major exit channel product in quenching collision, while the energy transfer for $Mg(^1P-^3P)$ spin change was not detectable.[15] However, fundamental data such as the reaction barrier, the branching ratio for the chemical and physical quenching, and the temperature effect on the quenching efficiency are still greatly lacking. This work is aimed to conduct these measurements.

In this work, a pump–probe method is employed to determine the thermal rate coefficients of $Mg(3\,^1P_1)$ by collisions with CH_4. The current method is better than the direct measurement of fluorescence decay as a function of quencher pressure. The latter measurement might be bothered by the radiation trapping effect. As reported, the radiation trapping could prolong the measured natural lifetime of $Mg(3\,^1P_1)$ from 1.9 ns to 100–120 ns.[15] The temperature dependence of total quenching rate coefficients is measured over the range from 660 to 850 K. According to the Arrhenius theory, the data obtained are substantially attributed to the chemical reaction with a potential barrier of $-(5.75–6.54)$ kcal mol^{-1}. Coupled with the *ab initio* results which find a large barrier to end-on attack, the negative energy dependence indicates that the reaction pathway is along the insertion coordinate, but without the slight potential barrier as reported in the aforementioned studies. Since the effective collision depends on the approach orientation, a simple angle-dependent collision model has been employed to account for the obtained kinetic data.

II. EXPERIMENT

An apparatus similar to the one employed in this work has been described elsewhere,[11–13] so only modification for the present experiment will be described here.

The pump–probe technique is composed of two tunable dye lasers, which were pumped, respectively, by a frequency-doubled and frequency-tripled Nd:YAG laser operating at 10 Hz with pulse duration of 5–8 ns. One dye laser was operated with mixed dyes of rhodamine 590 and rhodamine 610 in a 4:1 volume ratio. The output wavelength of this laser was then frequency doubled through a KDP crystal emitting at 285.2 nm, which was used to excite the Mg vapor in the $3s3p\,^1P_1$ state. The other dye laser, operated with coumarine 440 emitting at 435 nm, was used to probe the $Mg(3\,^1P_1)$ population in the $3s3p\,^1P_1–3s6d\,^1D_2$ transition. The nonresonant atomic fluorescence in the $3s5d\,^1D_2–3s3p\,^1P_1$ transition at 470 nm was detected in order to avoid spectral interference with the incident laser wavelength. The energy of the unfocused pump beam was maintained about 100 μJ for the $Mg(3s3p\,^1P_1)$ excitation, while the unfocused probe beam was about 50–80 μJ. Each beam was propagated in the opposite direction through an individual pinhole of 10 mm^2 cross section.

Although the energy of the pump laser was kept as low as possible, a weak atomic emission in the $3s4s\,^3S–3s3p\,^3P$ transition at 517 nm was still detectable. A similar problem was found in our previous work and elsewhere.[10,13] The emission interference might be attributed to resonant two-photon ionization of Mg by the pump laser, followed by recombination and relaxation or electron impact excitation. As it opens the channels for the additional higher lying atomic states populated by the pump laser alone, these collision-induced processes might contribute to the observed fluorescence on the $5d–3p$ transition and make the kinetic rate equations, describing the $3p$ population, more complicated. However, these processes were slow, especially for a low pressure condition, and their influence might become significant in a large delay time. For the experimental conditions applied, the fluorescence decay could be characterized exponentially, and therefore interference caused by the processes seems to be negligible in our case.

The reaction chamber was a stainless steel six-armed heat-pipe oven, in which the Mg metal was deposited in the reservoir and heated to a temperature of about 650 K. The Mg vapor pressure in equilibrium corresponded to 1.5 mTorr or 2×10^{13} atoms/cm^3. Mg metal chips were refluxed in the oven at 750 K for about 2–3 h before kinetic measurement. The temperatures of the reactor and the Mg reservoir were measured and regulated by two thermocouples and temperature controllers, respectively. Because parts of the reservoir and reactor were in good thermal contact, the reservoir temperature might rise with the increase of the reactor temperature. In our case, even though the reactor temperature was increased to 850 K, the reservoir temperature might be controlled as low as about 700 K. The generated Mg vapor pressure was still low enough to keep the pseudo-first-order approximation valid.

Methane was the only quencher in the study, but Ar was introduced as a bath gas to keep the methane thermally homogeneous. Methane, 99.999% purity (Matheson), and argon, 99.999% purity (Matheson), were used without further purification. The two gases were regulated by an individual mass flow controller (Sierra Instruments, model 820), well mixed, and then entered the chamber through five side arms. This process ensured that the CH_4 and Ar gases would be mixed well in the oven chamber and that particle deposition on the optical windows would be safely avoided.

Following the $Mg(3\,^1P_1)$ excitation in the presence of excess CH_4 and Ar bath gas, the atomic laser-induced fluorescence (LIF) of $Mg(3\,^1P_1)$ was probed as a function of the time delay between pump and probe beams. The delay time is defined as zero when the falling edge of the pump–laser pulse comes into contact with the rising edge of the probe–

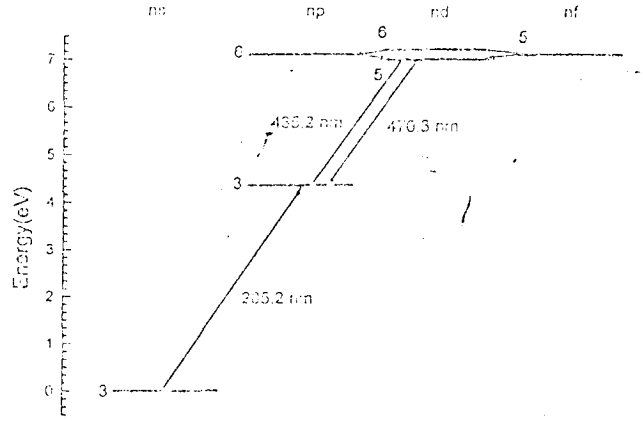

FIG. 1. Atomic energy diagram of Mg. The pump–probe scheme is also displayed with fluorescence detection in the $3s5d\ ^1D_2-3s3p\ ^1P_1$ transition.

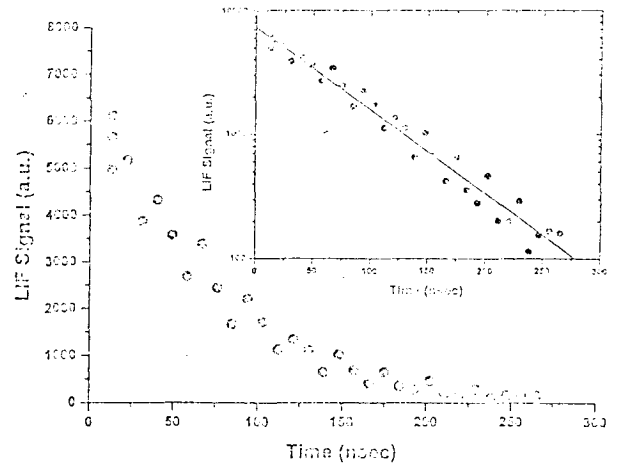

FIG. 2. The Mg atomic LIF decay with the time delay between pump and probe laser pulses. The conditions for the measurement are at temperature 660 K, total pressure 2.5 Torr, and CH_4 concentration 1.29×10^{15} molecule cm^{-3}. Inner panel: Semilogarithmic plot of LIF signal vs delay time. The slope by least-squares fit gives the pseudo-first-order rate coefficient of $2.92\times10^6\ s^{-1}$.

laser pulse. The resulting Mg atomic LIF signal was focused onto a monochromator with a single lens and detected by an attached photomultiplier tube. The grating of the monochromator was set at 470 nm to allow for transmission of a 2 nm spectral bandwidth, when the slits were open to 1000 μm. The LIF signal as a function of time delay was then processed by a transient digitizer (Tektronix, 2432A). To improve the signal-to-noise ratio, each time-resolved spectrum was averaged over 30 traces, and the whole profile was then integrated within a gated width of 400 ns. The data were stored in a personal computer for further treatment.

Figure 1 shows a partial energy-level diagram for Mg[17] and the related transitions for excitation and emission processes. The $3s5d$ state may be populated through radiative or collisional relaxation from $3s6d$ or the intermediate states $3s6p$ and $3s5f$. Thanks to the short lifetimes of these upper states, the involved processes relaxing to the $3s5d$ state have been completed within the 400 ns gated time and the temporal evolution of the $3s5d$ population may decay exponentially with the time delay. The CH_4 pressures were regulated in the range from 20 to 500 mTorr, corresponding to $3\times10^{14}-6\times10^{15}$ molecule cm^{-3} in the study. Figure 2 shows an example of time-resolved LIF decay of $Mg(3\ ^1P_1)$ in the presence of a total pressure of 1.3 Torr which contains 4.74×10^{15} molecule cm^{-3} CH_4 at 660 K. The corresponding effective lifetime may be derived from the slope of the semilogarithmic plot.

III. RESULTS AND DISCUSSION

A. Temperature dependence of the rate coefficients

The depletion of the $Mg(3s3p\ ^1P_1)$ population by CH_4 collision in the Ar bath gas may be described in the following schemes:

$$Mg(3s3p\ ^1P_1)+Ar\rightarrow Mg(3s^2\ ^1S_0)+Ar, \quad (1a)$$

$$Mg(3s3p\ ^1P_1)+CH_4\rightarrow Mg(3s^2\ ^1S_0)+CH_4, \quad (1b)$$

$$Mg(3s3p\ ^1P_1)+CH_4\rightarrow MgH(X\ ^2\Sigma^+)+CH_3, \quad (1c)$$

$$Mg(3s3p\ ^1P_1)\rightarrow Mg(3s^2\ ^1S_0)+h\nu. \quad (1d)$$

The related differential rate equation is expressed as

$$\frac{-d[Mg]}{dt}=-\{k_{1a}[Ar]+(k_{1b}+k_{1c})[CH_4]+k_{1d}\}[Mg]. \quad (2)$$

In our study, we had kept the $Mg(3\ ^1P_1)$ population density low enough to avoid the self-quenching phenomenon. To apply a pseudo-first-order approximation, we control the partial pressure of CH_4 to be much larger than that of $Mg(3\ ^1P_1)$ and the total pressure of the system, containing excess Ar bath gas, was maintained constant. The pseudo-first-order decay coefficient, k', is defined as

$$k'=(k_{1a}[Ar]+k_{1d})+(k_{1b}+k_{1c})[CH_4] \quad (3)$$

and its value may be determined from the effective lifetime of the atomic LIF decay of the $Mg3\ ^1P_1$ state. Like the example given in Fig. 2, the LIF decays at fixed pressures of CH_4 are exponential with the delay time between pump and probe laser pulses, and their shapes may be fitted to the form of $A\exp(-k't)$. The corresponding effective lifetime may thus be evaluated from the semilogarithmic plot of the decay. The plot of the reciprocal of the effective lifetime, equivalent to k', against $[CH_4]$ yields the intercept, $(k_{1a}[Ar]+k_{1d})$, and the slope, $k_{1b}+k_{1c}$. Within the temperature range given, the resulting Mg density may lead to radiation trapping, such that the effective lifetime of $Mg(3\ ^1P_1)$ is prolonged.[15] Since the Ar quenching rate coefficient is negligible as compared to CH_4,[15] and the obtained intercept is small, in Fig. 3, $k'-(k_{1a}[Ar]+k_{1d})$ vs $[CH_4]$ is plotted over the temperature range of 660–850 K to measure temperature dependence. The slopes of these plots under different temperatures yield the total deactivation rate coefficients, $k_{1b}+k_{1c}$. These data, with 2σ statistical errors from a linear regression fit to each plot, are listed in Table I. In order to examine the reliability of the above method for the effective lifetime detection (Fig. 2), we also monitored the resonance fluorescence from the $3s6d$ to $3s3p$ states at 435 nm at 680 K. The obtained rate

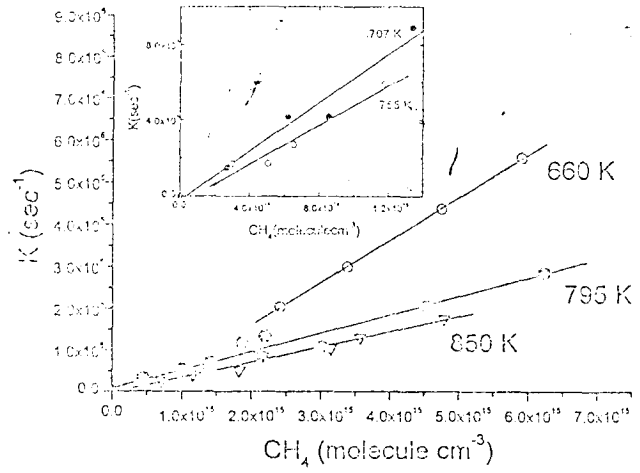

FIG. 3. The plot of K, which is defined as $k'-(k_{1a}[\mathrm{Ar}]+k_{1d})$, against $[CH_4]$ at different temperatures. Each slope by least-squares fit gives the second-order rate coefficient.

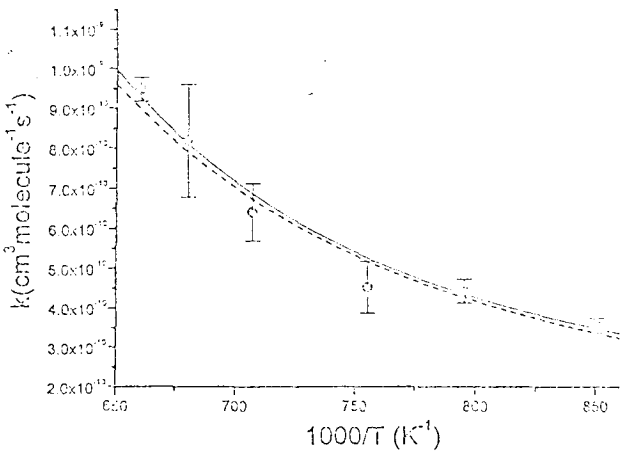

FIG. 4. Temperature dependence of the total quenching rate coefficient, k, for the Mg($3\,^1P_1$) atom by CH_4 collision. The solid line indicates the curve fitting to the form of $a+b\exp(-E/RT)$; the dashed line indicates the curve fitting to the form of $b\exp(-E/RT)$ alone.

coefficient was consistent with that evaluated in Table I within 10% deviation. Thus the complication possibly resulting from the reactions initiated by the $3s6d$ state seems negligible in the kinetic rate determination.

The behaviors of physical and chemical quenchings have a different response to temperature variation. The temperature dependence of the physical quenching rate is usually insignificant, especially when the attractive force is dominant. For instance, based on the orbiting model, if the long-range potential is $-C_n/R^n$, the collision cross section for an entrance-channel controlled process can be correlated with the relative collisional energy to a power of $-2/n$.[15,18] The corresponding rate coefficient may be evaluated by integrating the cross section over the full range of collision energies. Two cases are exemplified in the following:[19] (1) For the case of ion-induced dipole interaction, i.e., $n=4$, the resulting rate coefficient becomes temperature independent. The (2) When the interaction of two neutral molecules is dominated by the potential with $n=6$, the rate coefficient is found to depend on the temperature to a power of 1/6. These results reveal that in most cases the temperature factor has little influence on the collision rate coefficients.

In sum, the temperature dependence for the obtained rate coefficients of total deactivation can be characterized by the formula, $k_{1b}+k_{1c}=a+b\exp(-E/RT)$. The first term, related to physical quenching, is assumed to be temperature independent, whereas the second indicates the chemical quenching described by the Arrhenius expression. The values for a fit to the plot of total deactivation rate coefficient versus temperature are: $a=(6.68^{+0.5}_{-1.0})\times10^{-11}$ cm^3 molecule^{-1} s^{-1}, $b=(5.88^{+0.1}_{-0.5})\times10^{-12}$ cm^3 molecule^{-1} s^{-1} and $E=(-6.54^{+0.2}_{-0.2})$ kcal mol^{-1} (Fig. 4, the solid line). The decrease of temperature from 850 to 660 K leads to an increase of the ratio of the chemical to the physical quenching from a factor of 5 to 14. Since the contribution of physical quenching is relatively small, the kinetic data may be fitted alternatively using the Arrhenius expression of $b\exp(-E/RT)$ alone. The plot in Fig. 4 (the dashed line) yields a goodness-of-fit comparable to that in Fig. 4 (the solid line) and the fit gives rise to $k_{1c}=(1.12\pm0.04)\times10^{-11}\exp(5.75\pm1.16$ kcal mol^{-1}/RT)cm^3 molecule^{-1} s^{-1}. The neglect of k_{1b} apparently has not had much of an affect on the fitted values. This phenomenon reveals the obvious dominance of the chemical reaction over the Mg($3\,^1P_1$) depletion channels by the CH_4 collisions. The quenching behavior of Mg($3\,^1P_1$) by CH_4 has been considered to be entrance channel controlled.[15] Between the entrance and the exit channel must exist sufficient coupling to let the electronic energy of the excited state be effectively dissipated. Our results indicate that the chemical reaction is the main exit channel. It is worthwhile to note that the thermal rate coefficients are subject to a negative temperature dependence, which indicates that the collision process should be along the attractive surfaces with a depth-well intermediate state.

TABLE I. Experimental determination of thermal rate coefficients k of Mg($3\,^1P_1$) by CH_4 collision as a function of temperature.[a]

T(K)	$k(10^{-10}$ cm^3 molecule^{-1} s^{-1})	T(K)	$k(10^{-10}$ m^3 molecule^{-1} s^{-1})
660	9.48±0.30	755	4.53±0.65
680	8.19±1.42	795	4.43±0.30
707	6.40±0.72	850	3.57±0.18

[a]Quoted uncertainty is 2σ.

The chemical interaction of Mg atom insertion into the C–H bond has been demonstrated to be the main pathway leading to the MgH product, of which the rotational distribution is characteristic of a bimodal feature.[7,10,13,14,16] As mentioned earlier, such rotational bimodality originates from the same insertion mechanism, irrespective of the entrance channel geometry. In accordance with Kleiber and co-workers' suggestion,[10] we have recently calculated two-dimensional potential energy surfaces (PESs), when Mg approaches in between two H atoms, and Mg and HCH are coplanar.[13] We found that a nonadiabatic transition had to take part in the reaction to obtain MgH in the $^2\Sigma^+$ state. The low-N and high-N components of the MgH distribution depended on the anisotropic interaction of the final state in the exit channel. The high-N states were anticipated to result from the path-

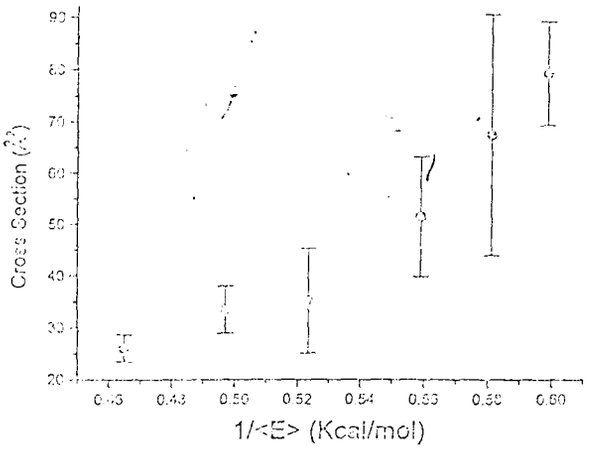

FIG. 5. The plot of total cross section for collisional deactivation against the reciprocal of the relative collisional energy. The cross section is given by the corresponding thermal rate coefficient divided by a mean relative velocity of the colliders, which is $\sqrt{8k_BT/\pi\mu}$.

way that the $HMgCH_3$ collision complex went through—a C_{3v} configuration—before decomposition, whereas the low-N states were formed through the pathway with weaker angular dependence of the potential interaction. By analogy with this case, $Mg(3\,^1P_1)$ with H_2 reaction also leads to a bimodal rotational distribution of MgH.[5,8,9,11,12,20] The subsequent microscopic reaction pathways are similarly dominated by insertion.

Breckenridge and co-workers have investigated the quenching efficiency of the $Mg(3\,^1P_1)$ state by a series of simple gases.[15] They found that except for the inert gases and the perfluoroalkanes, the cross sections were approximately gas kinetic and correlated well with the C_6 long-range force coefficient to a power 0.48 ± 0.05. The obtained value was larger than the prediction of an orbiting model with entirely dispersive long-range force, but could be consistent with an effective potential with a radial dependence between $1/R^6$ and $1/R^4$. Among the saturated and unsaturated hydrocarbons studied, CH_4 was the only quencher with a cross section lower than expected from the C_6 correlation. It was rationalized that a slight chemical barrier might exist for CH_4, but not for the other hydrocarbons.[15]

Since the temperature dependence of the thermal rate coefficients is available, it is worthwhile to examine the applicability of the orbiting model and absorbing-sphere model. Figure 5 shows the plot of the total quenching cross sections against the reciprocal of mean relative collisional energy. The fact that the data cannot be fitted to a straight line implies the invalidity of the absorbing-sphere model in this case. On the other hand, they are not suitable for the orbiting model—which neglects the influence of the reaction orientation. In fact, the chemical reaction in the $Mg(3\,^1P_1)-CH_4$ system will not take place unless the collisions approach the surface crossing region between the excited and the ground state surfaces.

By using a self-consistent field level, Chaquin and coworkers have evaluated the energy barrier along the reaction coordinate to be <6.9 kcal mol^{-1}.[16] The slight barrier, however, has not appeared in our observation of temperature dependence. As pointed out by the authors, the estimated barrier may be lowered considerably provided that a higher calculation level is conducted or the zero-point energy of the departing C–H bond is considered.[16] Their study also shows the existence of a bound state with a productlike structure $MgH\cdot CH_3$ along the reaction coordinate, which lies 12.9 kcal mol^{-1} below the reactants.[16] This singlet bound state, having a small energy gap from the triplet state, enhances the strength of the singlet-to-triplet coupling,[19] thereby accounting for the strong triplet Mg emission observed with the use of Xe-matrix isolation at 12 K.[21] In this work, the resultant negative temperature dependence of the thermal rate coefficients lends support to the prediction of such a bound state, although the observed value is about twice as small as the theoretical energy estimation. In an attempt to find the position of the bound state along the reaction coordinate, it is worthwhile to relate the calculated intermediate structure[16] with two-dimensional PES information.[13] The above bound-state $MgH\cdot CH_3$ is found to be equivalent to the structure of the collision complex in the region of surface crossing. The bond lengths of Mg–H, Mg–C, and C–H in the former structure are 1.75, 2.67, and 2.73 Å, while the corresponding values in the latter one are 1.74, 2.63, and 2.8 Å, respectively. Their geometric structures are in agreement within 5% deviation. It therefore can be affirmed that the bound state is located in the region of surface crossing, since the chemical reaction may not occur unless the nonadiabatic transition is involved.

B. Molecular collision models for the $Mg(3\,^1P_1)+CH_4$ reactions

In this work, we have attempted to fit two simple collision models in the current system. One is a simple collision theory (SCT).[19] Its rate coefficient may be expressed as

$$k_{SCT}(T)=P\pi d^2(8k_BT/\pi\mu)^{1/2}\exp(-E_0/k_BT), \qquad (4)$$

where d is the hard-sphere collision radius; E_0, the energy barrier along the line of centers, which remains constant in the collision irrespective of the orientation; μ is the reduced mass; k_B is the Boltzmann constant, and P is the steric factor. In the equation, the reactants are considered structureless, so that the colliding orientation may not influence the reaction probability. When applying the model, we adopted $E_0=-5.75$ kcal mol^{-1} determined in this work and $d=2.45$ Å for the sum of effective radii of Mg and CH_4. As the steric factor is adjusted to 0.012, a fit is shown in Fig. 6 for the temperature dependence of the rate coefficients. In addition, Eq. (4) is derived by considering the reaction probability as $(1-E_0/E_T)$, where E_T is the relative collisional energy. It becomes questionable to adopt a negative threshold energy in the equation. Although the model fails to apply, the existence of the steric factor might suggest that the anisotropy of the PES should not be ignored.

The other model employed is the angle-dependent line of normals model (ADLN).[19,22] This model attempts to improve the crude isotropic energy barrier of SCT by defining the potential hypersurface to be angle dependent,

$$\epsilon_{th}=\epsilon_{th}^0+2\epsilon'(1-\cos\phi), \qquad (5)$$

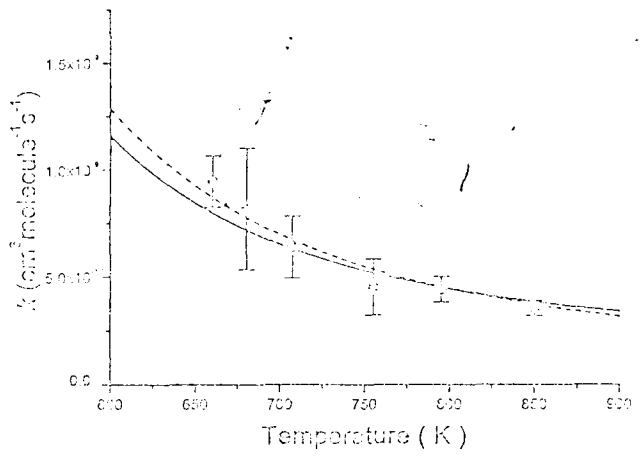

FIG. 6. Curve fit of kinetic data as a function of temperature with the models SCT (the dashed line) and ADLN (the solid line).

where ϕ is the activated complex bond angle for the colliding system; $\epsilon_{\rm th}^0$ is the threshold energy as $\phi=0$ (i.e., the collision geometry is in the C_{3v} symmetry for the current system); ϵ' is a fitting parameter. The resulting reaction rate coefficient is given as

$$k_{\rm ADLN}(T)=2\pi D^2\left(\frac{8kT}{\pi\mu}\right)^{1/2}\int_0^{\pi/2} e^{-\epsilon_{\rm th}(\phi)/kT}(\sin\phi)\times(\cos\phi)d\phi, \tag{6}$$

where D is the soft-shell reactive radius in the activated complex. In the simulation, we adopted the following values: $D=2.45$ Å, equivalent to the hard-sphere collision radius as described above, and $\epsilon_{\rm th}^0=32.8$ kcal mol^{-1}, evaluated by Chaquin and co-workers[14] in a head-on C_{3v} collision configuration. Under the condition $\epsilon'=-21.6$ kcal mol^{-1}, the rate coefficient measurement may be perfectly fitted (Fig. 6). The predicted threshold energy in Eq. (6) decreases as the angle increases. The tendency is qualitatively consistent with the *ab initio* PES calculation, which reveals that the Mg approach in between two H atoms of CH_4 is energetically favored.[13,16] But it should be noted that the ADLN fit is rough and yields no further information. The model at best reflects a detailed treatment of the steric factor by angular integration over the anisotropic energy barrier.

IV. CONCLUSION

We have obtained the thermal rate coefficients of $Mg(3s3p\ ^1P_1)$ by CH_4 collisions in the presence of Ar bath gas as a function of temperature in the range of 660–850 K. The depletion processes are attributed to physical and chemical quenching. The former contribution is evaluated to be less than 6.7×10^{-11} cm^3 molecule^{-1} s^{-1}, while the latter one is $(0.59-1.12)\times10^{-11}\exp(5.75-6.54\ \text{kcal mol}^{-1}/RT)$cm^{3}molecule^{-1} s^{-1}. The negative temperature dependence of the measurement indicates the existence of a depth-well intermediate, which is anticipated to locate in the region of surface crossing between the excited and the ground states. Since the reaction is characterized by the anisotropic PES interaction, the orbiting and absorbing-sphere models cannot be validly applied. The ADLN fit to the kinetic data for the temperature dependence is consistent with the insertion mechanism reported, which shows energetic preference to the end-on attack.

ACKNOWLEDGMENTS

The authors wish to thank Dr. D. K. Liu and Y. R. Ou for helpful discussions. This work is financially supported by the National Science council of the Republic of China under Contract No. NSC 87-2113-M-001-021.

[1] B. L. Earl and R. R. Herm, J. Chem. Phys. 60, 4568 (1974).
[2] B. L. Earl, R. R. Herm, S. M. Lin, and C. A. Mims, J. Chem. Phys. 56, 867 (1972).
[3] D. K. Liu and K. C. Lin, J. Chem. Phys. 105, 9121 (1996).
[4] D. K. Liu and K. C. Lin, J. Chem. Phys. 107, 4244 (1997).
[5] W. H. Breckenridge and H. Umemoto, J. Chem. Phys. 80, 4168 (1984).
[6] W. H. Breckenridge and H. Umemoto, J. Chem. Phys. 81, 3852 (1984).
[7] W. H. Breckenridge and H. Umemoto, J. Chem. Phys. 77, 4464 (1982).
[8] P. D. Kleiber, A. M. Lyyra, K. M. Sando, V. Zafiropulos, and W. C. Stwalley, J. Chem. Phys. 85, 5493 (1986).
[9] P. D. Kleiber, A. M. Lyyra, K. M. Sando, S. P. Heneghan, and W. C. Stwalley, Phys. Rev. Lett. 54, 2003 (1985).
[10] T. H. Wong and P. D. Kleiber, J. Chem. Phys. 102, 6476 (1995).
[11] K. C. Lin and C. T. Huang, J. Chem. Phys. 91, 5387 (1989).
[12] D. K. Liu, T. L. Chin, and K. C. Lin, Phys. Rev. A 50, 4891 (1994).
[13] D. K. Liu, Y. R. Ou, and K. C. Lin, J. Chem. Phys. 104, 1370 (1996).
[14] W. H. Breckenridge, J. Phys. Chem. 100, 14840 (1996).
[15] W. H. Breckenridge and H. Umemoto, J. Chem. Phys. 75, 698 (1981).
[16] P. Chaquin, A. Papakondylis, C. Giessner-Prettre, and A. Sevin, J. Phys. Chem. 94, 7352 (1990).
[17] A. A. Radzig and B. M. Smirnov, *Reference Data on Atoms, Molecules, and Ions* (Springer, Berlin, 1985).
[18] J. E. Velazco, J. H. Kolts, and D. W. Setser, J. Chem. Phys. 69, 4357 (1978).
[19] I. W. M. Smith, *Kinetics and Dynamics of Elementary Gas Reaction* (Butterworths, London, 1980), pp. 68–73.
[20] Y. R. Ou, D. K. Liu, and K. C. Lin, J. Chem. Phys. 108, 1475 (1998).
[21] J. G. McCaffrey and G. A. Ozin, J. Chem. Phys. 89, 1844 (1988).
[22] F. L. Wiseman and A. G. Rice, J. Chem. Educ. 70, 914 (1993).

Ab initio calculation for potential energy surfaces relevant to the bimodal rotational distribution for $Mg(3s3p\,^1P_1)+H_2 \rightarrow MgH(^2\Sigma^+)+H$

Yaw-Ren Ou, Dah-Kuo Liu, and King-Chuen Lin[a)]
Department of Chemistry, National Taiwan University, Taipei, Taiwan 106, and Institute of Atomic and Molecular Sciences, Academia Sinica, P.O. Box 23-166, Taipei, Taiwan 106, Republic of China

(Received 12 August 1997; accepted 13 October 1997)

Two *ab initio* methods have been employed to calculate the dynamical potential energy surfaces (PES's) for the excited ($^1B_2$ or $^1A'$) and the ground ($^1A_1$ or $^1A'$) states in the $Mg(3s3p\,^1P_1)$–H_2 reaction. The obtained PES's information reveals that the production of MgH in the $^2\Sigma^+$ state, as $Mg(^1P_1)$ approaches H_2 in a bent configuration, involves a nonadiabatic transition. The MgH_2 intermediate around the surface crossing then elicits two distinct reaction pathways. In the first one, the bent intermediate, affected by a strong anisotropy of the interaction potential, decomposes via a linear HMgH geometry. The resulting MgH is anticipated to populate in the quantum states of rotational and vibrational excitation. In contrast, the second pathway produces MgH in the low rotational and vibrational states, as a result of the intermediate decomposition along the stretching coordinate of the Mg–H elongation. These two tracks may account for the previous experimental findings for the MgH distribution, which the impulsive model has failed to comprehend. By far, different interpretations have been proposed especially for the low-N MgH product. The supply of a detailed PES's information in this work helps to clarify the ambiguity. It is also conducive to an interpretation of the isotope and temperature effects on the product rotational distribution. © *1998 American Institute of Physics.* [S0021-9606(98)00104-4]

I. INTRODUCTION

The nascent MgH product has been found to yield a bimodal rotational population distribution in the reaction of $Mg(3s3p\,^1P_1)$ with H_2.[1–6] The reaction pathways to cause such a rotational bimodality has been an issue of concern. As HD was used to replace H_2, the reaction led to an identical MgH rotational distribution. The lack of the isotope effect suggests that the bimodality should originate from a side-on attack of Mg insertion into H_2.[2] In the studies of potential energy surfaces (PES's) calculation, Blickensderfer *et al.* and Chaquin *et al.* have reported that the reaction coordinate for the insertive mechanism tracks an attractive $^1B_2$ surface.[7,8] The latter group further demonstrated that the H-abstraction mechanism along a collinear geometry suffered from a substantial energy barrier.[8] The domination of the Mg insertion mechanism was also supported in our experiment of temperature dependence, in that the MgH rotational distribution was little affected with the temperature variation.[3] It is generally anticipated that the $Mg(^1P_1)$ plus H_2 reaction is exit-channel controlled, causing the MgH rotational bimodality through two distinct microscopic pathways. By analogy with this reaction, Kleiber and co-workers studying the $Na(4p^2P)$–H_2 reaction have found a similar rotational bimodality for the NaH product.[9,10] Since there was no kinematic isotope effect on the rotational distribution, the bimodal nature was anticipated to stem primarily from a side-on attack along an attractive surface, which determined the microscopic branching late in the exit channel.

In our recent study of the microscopic branching leading to the MgH product, we have found that two distinct types of reaction dynamics are responsible for the low-N and high-N production.[4] One type produces MgH in lower rotational levels and preferentially $v''=0$, and the other type produces MgH in higher rotational levels with comparable $v''=0$ and $v''=1$ populations.[4] The impulsive model has been adopted for a tentative interpretation on the formation of bimodality. Accordingly, for the major reaction pathway, the H atom is expected to escape from a bent MgH_2 configuration, in which the bending mode initially activated may couple with the asymmetric stretching mode. The energy transfer into the asymmetric stretching mode facilitates the removal of the H atom and causes an effective vibrational motion of the remaining MgH. In addition, a torque is exerted upon MgH to excite the rotational population. As for the minor reaction pathway, the H atom should depart from a linear HMgH intermediate, of which the Mg atom lies in the center. The linear structure in the ground state has been identified to be stable at 12 K.[11] Thus the excess energy carried in the intermediate is presumed to have dissipated before decomposition, and thereby the resulting MgH may stay in the quantum states of low rotation and low vibration.[4]

It should be noted that the impulsive model[12–14] accounts for the breaking apart between the single atom and the remaining diatomic molecule in a three-atom system depending upon the initial bond angle. It ignores the influence of the bond angle variation along the reaction coordinate, and oversimplifies the treatment of potential interaction by using a diatomic potential term instead of a real PES.[15,16] Although the model is easy to follow and sometimes provides satisfactory explanation for the product rotational distribution, its reliability is questionable for the lack of a PES

a)Author to whom correspondence should be addressed. Fax: 886-2-3621483; electronic mail: kclin@hp9k720.iams.sinica.edu.tw

 0021-9606/98/108(4)/1475/10/$15.00

calculation. For instance, it fails to explain the dramatic difference of the rotational state distributions between OH $^2\Sigma$ and $^2\Pi$ states, as photodissociated from the respective $\tilde{B}\ ^1A_1$ and $\tilde{A}\ ^1B_1$ states of H_2O, in which the initial bond angles are identical for both states.[15,17,18] In the $Mg(3^1P_1)$ plus H_2 reaction, decomposition of a bent MgH_2 structure through a linear geometry may probably lead to rotational and vibrational excitation. However, our previous interpretation, based on the impulsive model neglecting the influence of the angle variation, simply attributed the formation of low-N component of the MgH distribution to the H-atom release directly from a linear intermediate.[4] In contrast, the high-N component was anticipated to result from the H-atom departing from the bent MgH_2 structure. In the explanation, it is assumed that the restoring force is exerted along the H–H coordinate; the Mg atom is treated as a spectator without taking part in the dissociation process. Nevertheless, this assumption turns out to be against the observation of the aforementioned isotope effect.[2] To calculate the related *ab initio* potential energy surfaces is apparently of vital importance to a deep understanding of the reaction mechanisms associated with the rotational bimodality.

Although Breckenridge and co-workers have first suggested that the MgH product rotational distribution should be determined by exit channel dynamics on an anisotropic PES for a decade,[1,2,7] there still lacks a detailed dynamical PES to quantify the related microscopic branching. In this work, we employ two methods of CIS and complete active space self-consistent field (CASSCF) levels to carry out *ab initio* calculation of the dynamical PES's for the excited and the ground states involved in the reaction of $Mg(3^1P_1)$ with H_2. The resulting PES's information supports the mechanism for the MgH production to be through a nonadiabatic transition as proposed previously.[1,4,7,8] However, the prediction of the pathways based on the PES's results is against those on the impulsive model.[1,4] As the $Mg(^1P_1)$ atom approaches H_2 along the $^1B_2$ potential surface, the bent intermediate near the crossing region has been found to decompose following two microscopic reaction processes. As the intermediate decomposition is affected by a strong anisotropy of the interaction potential, the MgH may be produced in the quantum states of rotational and vibrational excitation as observed previously.[1,4] In contrast, as the bent intermediate decomposes along the stretching coordinate of the Mg–H elongation, the pathway produces MgH in the low rotational and vibrational states. Especially for this portion of MgH distribution, different interpretations have been proposed but without the assistance of a detailed PES's information. Among these suggestions are the mechanisms via end-on attack of H-abstraction,[1] singlet-to-triplet curve crossing,[5] decomposition of a linear H–Mg–H complex,[3,4] and secondary collision between the rapidly rotating MgH and the product H atom.[1] This work is aimed to clarify the ambiguity from the theoretical point of view and to provide a reasonable interpretation of the isotope and temperature effects on the product rotational distributions.

TABLE I. Comparison of bond lengths and absolute energies of MgH ($^2\Sigma^+$) and linear HMgH intermediate ($^1\Sigma_g^+$).

Molecule	Bond length (Å)	Energy	Reference
MgH	1.735	−200.138 77[a]	this work
	1.726	−200.175 37[b]	this work
	1.726	−200.165 59[c]	this work
	1.735	−200.168 10[d]	this work
	1.681	−200.169 52	8
	1.731		20
HMgH	1.706	−200.720 48[a]	this work
	1.701	−200.784 37[b]	this work
	1.701	−200.769 90[c]	this work
	1.710	−200.773 55[d]	this work
	1.714	−200.776 66	8
	1.713	−200.786 70	21
		−200.715 57	22
		−200.783 86	23

[a]Calculated in the HF/6-31G** level.
[b]Calculated in the CISD/6-31G** level.
[c]Calculated in the MP2/6-31G** level.
[d]Calculated in the MP4/6-31G** level, the method adopted for single point computation of the ground PES in the text.

II. COMPUTATION PROCESSES

A. Method I: CIS

Two methods were employed to compute the potential energy surfaces for the $Mg(3^1P_1)+H_2$ and the $Mg(3^1S_0)+H_2$ systems. In the method I, we used basis sets of 6-31G** level for the Mg and H atoms. The configuration interaction (CI) calculation with single excitation (CIS) contained in the GAUSSIAN 92 program[19] was adopted to compute the $^1B_2$ excited state in C_{2v} symmetry, or $^1A'$ in C_s symmetry for the $Mg(^1P_1)+H_2$ reaction. On the other hand, a fourth-order Møller–Plesset (MP4) method was used to calculate the ground state ($^1A_1$ or $^1A'$) PES for the $Mg(^1S_0)+H_2$ system; the perturbative technique adopted the HF/6-31G** structure as the previous run. A point-by-point calculation was conducted over at least 625 grid points to form a two-dimensional PES each for the excited and ground states.

To test the reliability of the methods used, we computed the structure optimization for MgH ($^2\Pi$ and $^2\Sigma^+$) and HMgH ($^1\Sigma_g^+$ and $^1\Pi_g$). Some calculated bond lengths and total absolute energies are presented in Table I, of which the results are in agreement with those reported previously.[8,20–23] The dynamical PES's for the reactions of Mg ($^1S_0$, $^3P_1$, and $^1P_1$) with H_2 were evaluated in either C_{2v} or C_s approach geometry, and the results agree satisfactorily with those from Chaplin *et al.*[8] We also computed the $^1B_2$ and $^1A_1$ surfaces in the Mg–H_2 collisions as a function of bond angle and distance from Mg to the center of H_2. As these two parameters were varied in a linear proportion from the initial C_{2v} to the final $C_{\infty v}$ structure of MgHH, the singlet-to-triplet curve crossing occurred at 30°, a rotation angle of the H_2 molecule around its center. This is also consistent with the result reported by Chaplin *et al.*[8]

TABLE II. Comparison of the absolute energies calculated for $Mg+H_2$, MgH_2, MgH, and MgH+H in the varied states.[a]

$Mg+H_2$	CIPSI[b]	CASSCF[b]	ECI	CASSCF[c]
$1\,^1A_1$	−200.808 43	−200.773 399 1	−200.699 66	−200.773 368 9
$^3B_2$	−200.779 10	−200.680 579 5	−200.610 58	−200.680 641 3
$^1B_2$	−200.628 48	−200.663 549 6	−200.524 27	−200.663 604

MgH_2	CIPSI	ECI	CASSCF
$^1\Sigma_g^+$	−200.776 66	−200.673 03	−200.750 477 8
$^3\Pi_u$	−200.567 19	−200.474 91	−200.571 153 3
$^1\Pi_g$	−200.583 60	−200.469 82	−200.567 164 4

MgH	CIPSI	CASSCF
$^2\Sigma^+$	−200.169 52	−200.156 027 6
$^2\Pi$	−200.082 36	−200.070 496 2

MgH+H[d]	CIPSI	CASSCF
$^1\Sigma^+$	−200.587 19	−200.654 482 7
$^1\Pi$	−200.472 94	−200.567 007 8

[a]CASSCF calculation level adopted in this work; CIPSI and ECI adopted by Chaquin *et al.* (Ref. 8).
[b]H–H=0.74 Å; distance from Mg to the center of H_2=7.0 Å.
[c]H–H=0.74 Å; distance from Mg to the center of H_2=5.0 Å.
[d]MgH=1.714 Å (CIPSI and ECI); optimized MgH=1.740 Å (CASSCF).
[e]MgH=1.681 Å (CIPSI); optimized MgH=1.782 Å (CASSCF).
[f]MgH(1)=1.681 Å, Mg–H(2)=3.5 Å (CIPSI); MgH(1)=1.782 Å, Mg–H(2) =3.5 Å (CASSCF).

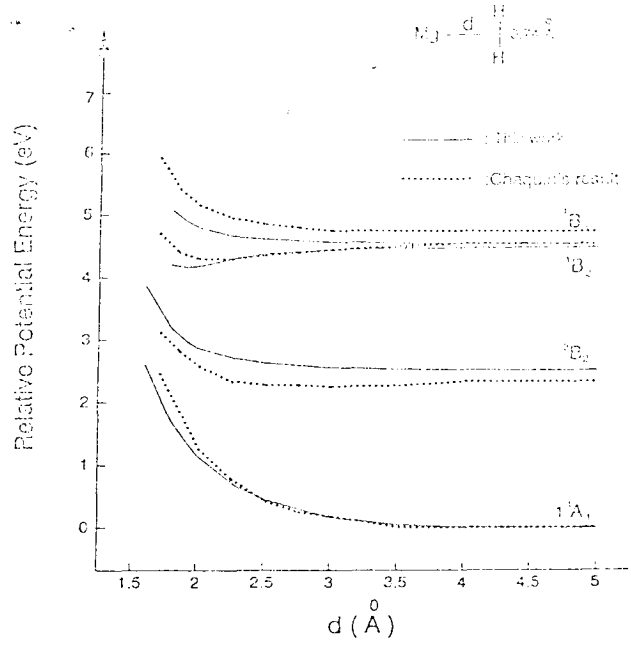

FIG. 1. The potential surfaces for the $1\,^1A_1$, $^3B_2$, $^1B_2$, and $^1B_1$ states, in comparison with those calculated by Chaquin *et al.*

B. Method II: CASSCF

In method II, we employed the CASSCF calculation level with a basis set of 6-31+G* to compute both the ground and the excited PES's for the $Mg+H_2$ reaction.[19,24] Four active electrons and six active orbitals were taken, and the total configurations amounted to 105, which contained not only single excitation but also double, triple, and quadruple excitations. A large increase in the configurations renders method II to be more reliable than method I.[24]

According to this method, the total absolute energies of $Mg+H_2$, MgH_2, MgH, and MgH+H in the varied states were calculated and compared to those reported,[8] as presented in Table II. The CASSCF calculation for the MgH ground state involved three active electrons, five active orbitals, and 40 configurations. The energy optimization for the MgH structure led to a value of 1.782 Å for the bond length and the energy difference of 2.33 eV between $^2\Pi$ and $^2\Sigma^+$ states. The results are consistent with the corresponding findings of 1.731 Å and 2.39 eV, determined from a pertinent emission spectrum.[25,26] For the MgH_2 ground state ($^1\Sigma_g^+$), we adopted four active electrons and six active orbitals in the CASSCF calculation. The optimized bond length of MgH and the total energy yielded a value of 1.7407 Å, and −200.750 48 a.u., respectively. A comparison was made with other results such as bond length of 1.714 Å and total energy of −200.776 66 a.u. from Chaquin *et al.*,[8] bond length of 1.713 Å from Ahlrichs *et al.*,[21] total energy of −200.715 57 a.u. from Pople and co-workers,[22] −200.786 and −200.788 67 a.u. from Ahlrichs *et al.*[21] using PNO-CI and CEPA methods, respectively, and −200.783 86 a.u. from Guest and Wilson.[23] The energies for the MgH_2 excited states ($^3\Pi_g$ and $^1\Pi_g$) were also computed, involving four active electrons, seven active orbitals, and 210 configurations. The obtained energies of the triplet and singlet state relative to the $^1\Sigma_g^+$ ground state were 4.88 and 4.99 eV, close to the values of 5.16 and 5.27 eV reported.[8]

As the $Mg(^1P_1)$ atom approaches H_2 in C_{2v} geometry, the energy level is split into $^1B_2$, $^1B_1$, and $^1A_1$ states. Among them, $^1B_2$ is the only state with an attractive potential, which is stabilized to some extent due to the electronic transfer from $3p_y$ to $\sigma^*_{H_2}$ in the overlap of these two orbitals.[1,8] As compared in Fig. 1, the calculated PES's for $Mg+H_2$ in the C_{2v} approach are consistent with those reported by Chaquin *et al.*[8] While the collision follows $^1\Pi$ or $2\,^1\Sigma^+$ PES's in the $C_{\infty v}$ approach, respectively, Chaquin *et al.* using an extended CI method have calculated the energy barrier to be 1.8 or 1.7 eV.[8] With method II, we obtained a corresponding barrier of 1.67 or 1.36 eV, as shown in Fig. 2. The calculated activation energy is obviously lowered, but there still exists a substantial barrier to prevent from an abstraction reaction along the $C_{\infty v}$ approach.

One should be noted that it becomes difficult to deal with the energy calculation for $Mg+H_2$ (C_s symmetry) near the crossing region, because of the electronic orbital interaction between the ground ($^1A'$) and the excited ($^1A'$) state. In our experience, to choose an appropriate HF wave function seems useful to improve the computation. However, for some grid points in the excited state around the crossing region, where the orbital mixing becomes serious, we have tried to increase the active orbitals up to 7–9, involving three unoccupied $4p$ orbitals of the Mg atom, but still failed to render the corresponding energy converged within 1×10^{-6} a.u.

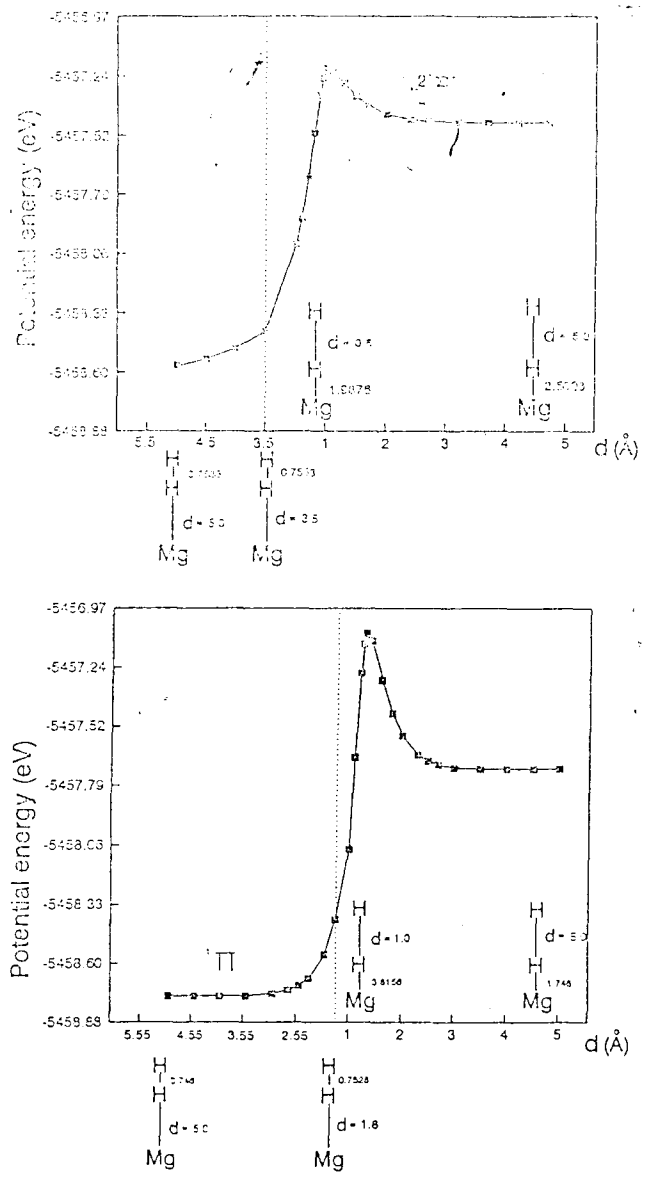

FIG. 2. The behavior of potential energy as $Mg(^1P_1)$ approaches H_2 in a collinear geometry. Note that an energy barrier existing in the $2\,^1\Sigma^+$ and $^1\Pi$ state to be 1.36 and 1.67 eV, respectively.

III. RESULTS AND DISCUSSION

A. Two-dimensional PES's by method I

In Fig. 3, method I was used to compute two-dimensional PES's for the ground ($^1A_1$ or $^1A'$) and excited states ($^1B_2$ or $^1A'$) in the Mg–H_2 reaction as a function of the bending angle α and the MgH distance d, while the other MgH bond was fixed at 1.7345 Å, an equilibrium distance calculated for the ground state. The parameters changed within the range, $35° \leqslant \alpha \leqslant 59°$ and $1.2\ \text{Å} \leqslant d \leqslant 3.96\ \text{Å}$. The upper and lower PES's cross at two regions. Figure 4 shows a detailed description of the equipotential contour of the ground PES, on which the surface crossings are marked. One crossing region (denoted as A) lies within the range of $47° \leqslant \alpha \leqslant 53°$ and $1.6\ \text{Å} \leqslant d \leqslant 2.0\ \text{Å}$, and the other (denoted as B) is within $52° \leqslant \alpha \leqslant 55°$ and $2.2\ \text{Å} \leqslant d \leqslant 2.7\ \text{Å}$. The MgH_2 structure around the larger region A is close to a C_{2v} geometry, having approximately equal bond distance. As the fixed MgH bond length was alternatively set to 1.4 or 2.1 Å, the corresponding equipotential contour calculated for the ground state showed the features similar to those in Fig. 4. Although the surface crossings in these cases may have different locations, the intermediate structures around the crossing regions tend to have a near-C_{2v} symmetry.

As mentioned earlier,[1,4,8] the $Mg(^1P_1)+H_2$ collision follows the attractive $^1B_2$ surface and ends up with the production of $MgH(^2\Sigma^+)+H$. The ground ($^1A_1$ or $^1A'$) and excited ($^1B_2$ or $^1A'$) PES's, associated with the $Mg(^1S_0)+H_2$ and $Mg(^1P_1)+H_2$ reactants, correlate symmetrically with the final products of $MgH(^2\Sigma^+)+H$ and $MgH(^2\Pi)+H$, respectively. Therefore, the nonadiabatic transition has to take part in the reaction in order to obtain MgH in the $^2\Sigma^+$ state.[1,4,8] As the $Mg(^1P_1)$ atom approaches H_2 in the C_{2v} geometry, the kinetic energy is initially deposited in the bending mode of HMgH, which may couple efficiently with the asymmetric stretching mode ($^1b_2$) to induce a vibronic transition;[1,4,8] the $^1B_2$–$^1A_1$ crossing transition is otherwise forbidden.

B. PES information associated with reaction pathways

Schinke *et al.*, without the assistance of a wave packet simulation, have successfully applied the PES calculation as a useful tool to comprehend photodissociation dynamics of polyatomic molecules.[15–17,27] The study reveals that, in the case of so-called "Franck-Condon mapping," in which the final state is weakly affected by the exit channel potential, the resulting product rotational distribution will primarily reflect the initial bending wave function of the parent molecule. But, in the "dynamical mapping," where the final state interaction cannot be ignored, the rotational distribution of the fragment becomes strongly dependent on the anisotropy of the potential energy surface in the exit channel. These concepts, which are known in the field of photodissociation dynamics, are also applicable to a full-collision event.[16] For an exit-channel controlled reaction like the Mg^*+H_2 system, the products are substantially affected by the final state interaction. The supply of a relevant PES information is therefore necessary for understanding the microscopic branching for the MgH population distribution.

To show an explicit relationship between the rotational angular momentum and a torque, we employed a Jacobi coordinate to define the intermediate structure in the Mg–H_2 collision. Under this frame, the variation of the rotational angular momentum in time is related to the torque generated, as expressed by[16,27]

$$\frac{dj}{dt} = -\frac{\partial V(\theta,R)}{\partial \theta}. \tag{1}$$

The equation describes how the rotational excitation depends upon the anisotropy of the relevant PES. Here R denotes the distance between the departing H atom and the center of mass for the MgH product, r is the bond length of MgH, and θ is the Jacobi angle between R and r axes.[16] Since the

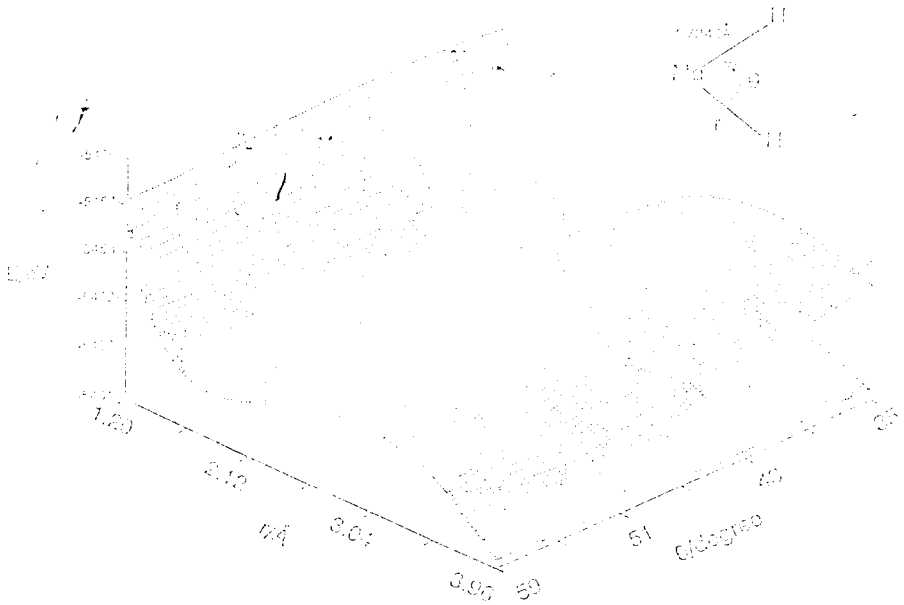

FIG. 3. Two-dimensional PES's for the ground ($^1A_1$ or $^1A'$) and excited states ($^1B_2$ or $^1A'$) in the Mg–H_2 reaction as a function of bending angle and bond distance between Mg and one H atom, while the other MgH bond was fixed at 1.7345 Å. The calculation was conducted with method I.

center-of-mass for MgH [illegible] almost coincidently in the position of the Mg atom, the Jacobi angle may be represented appropriately by the bond angle.

In Fig. 4, two main features may be found from the equipotential contour of the ground PES. First, the potential energy of the ground state rises up at a shorter Mg–H distance, then decreases gradually along the direction of Mg–H elongation. Such a tendency is irrespective of the bending angle. Second, as the angle exceeds about 50° with Mg–H distance close to 1.7 Å, the PES begins to show a strong angular dependence. Once the bending angle is increased to 180°, the potential surface rapidly falls down to the well, 3.8 eV below the reference energy of the $Mg(^1P_1)+H_2$ reactants. Accordingly, the MgH_2 complex is anticipated to follow two microscopic pathways to break apart. One tracks along the stretching direction to dissociate Mg–H, and the

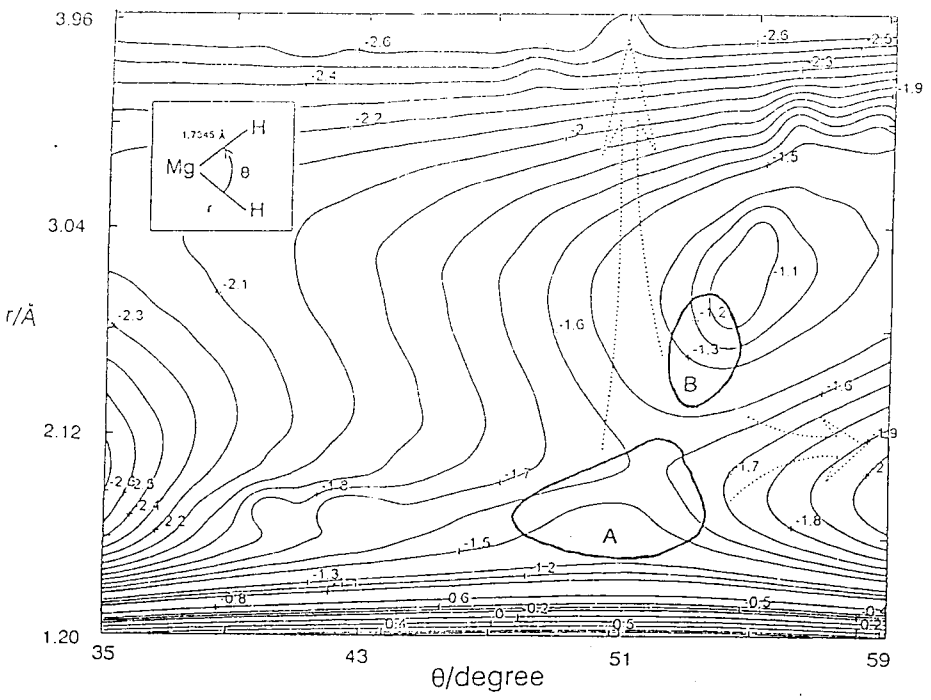

FIG. 4. The equipotential contour (relative energy in eV) of the ground state PES, on which the surface crossing regions with the lowest excited state are marked. The arrows are indicative of the probable exit-channel directions for the H-atom departing from the bent intermediate around the crossing regions.

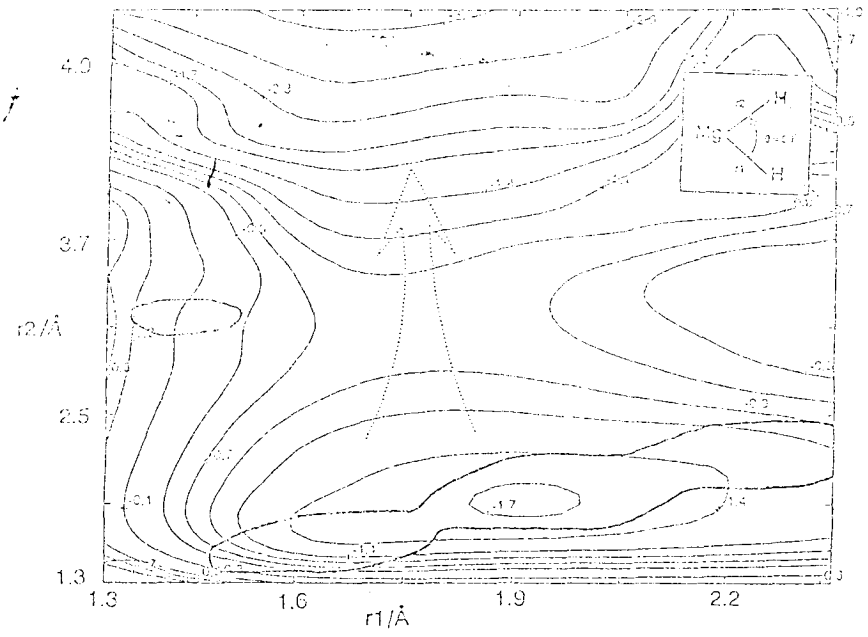

FIG. 5. The equipotential contour (relative energy in eV) of the ground state PES as a function of two Mg–H distances, while the bending angle is fixed at 50°. The heavy circles denote the surface crossing regions, and the arrow is indicative of the probable dissociation direction along the Mg–H coordinate.

other goes through the linear HMgH geometry before breaking apart. If the H atom is removed from the complex along directly the dissociation coordinate of Mg–H, as presented in Fig. 4, the angular dependence of the potential surface will become very weak. Equation (1) shows that the trajectory causes insignificant rotational excitation. Such a dissociation process also results in a weak coupling between the r_1 and r_2 coordinates; that is, when one bond distance r_2 of MgH is prolonged, the other one r_1 maintaining about 1.7–1.9 Å can be little perturbed, as shown in Fig. 5. The final MgH product thus obtained should lie in the low quantum states of rotation and vibration. In contrast, when the dissociation process follows the second trajectory passing through the linear geometry (Fig. 4), a strong angular dependence of the PES results in a large torque, which gives rise to rotational and vibrational excitation for the MgH product. Figure 6 gives a clear depiction of the two reaction pathways. One pathway accounts for the experimental findings for MgH in the lower rotational states and preferentially $v''=0$; the other leads to the higher rotational states with comparable $v''=0$ and $v''=1$ population.[4]

C. PES by method II

As shown in Fig. 7, the potential energies of MgH_2 ($^1B_2$ and $^1A_1$) in C_{2v} symmetry are calculated as a function of the bond length and the bond angle. The nonadiabatic transition may occur within the ranges of bond angle between 40° and 56° and bond distance roughly between 1.7 Å and 2.3 Å. When the angle is fixed at 52°, for instance, the surfaces cross at a Mg–H distance of 2.3 Å. Figure 8 shows the energy of the MgH_2 ground state as a function of bond angle and bond length, when the other bond length is fixed at the optimized distance ~1.7 Å calculated under a C_{2v} geometry. As the $Mg(^1P_1)$ approaches H_2 in a bent configuration, the MgH_2 intermediate is allowed for an effective nonadiabatic transition within a small crossing region as described above. From Fig. 8, the intermediate may be found to dissociate following two pathways. One is to track along the elongation coordinate of Mg–H, which leads to exothermicity at the bond angle <60°. The MgH thus obtained may lie in a low rotational distribution, since the bond angle of MgH_2 is weakly varied as it dissociates. The second pathway is toward the direction of the angle expansion, and thereby the corresponding energy tends to decrease. This channel favors to produce MgH in the higher rotational distribution.

Figure 9 shows the potential energy dependence of the MgH_2 ($^1A'$) ground state on the bond distance, as the bond angle is fixed at 52°. Similarly, the surface crossing is restricted to the range between 1.7 and 2.3 Å. As one bond distance is fixed at 1.775 Å, the MgH_2 becomes ready to dissociate along the MgH stretching coordinate. In this manner, the dissociation process may not disturb the bond angle, thus leading to the low-N MgH product. Furthermore, the bond length at 1.775 Å, close to the equilibrium distance of the product, is little changed during the dissociation. This favors to produce a low vibrational population. The increase of the fixed bond length will hinder the decomposition along the coordinate of MgH elongation. As shown in Fig. 9, when an energy barrier increases with the fixed bond length, the MgH_2 decomposition can follow only the direction via a linear geometry, and the resulting MgH product tends to populate in the higher rotational and vibrational states. Although Figs. 8 and 9 exhibit different aspects from the two-dimensional PES's (Figs. 4 and 5), they provide the same information on the reaction pathways for the MgH distribution.

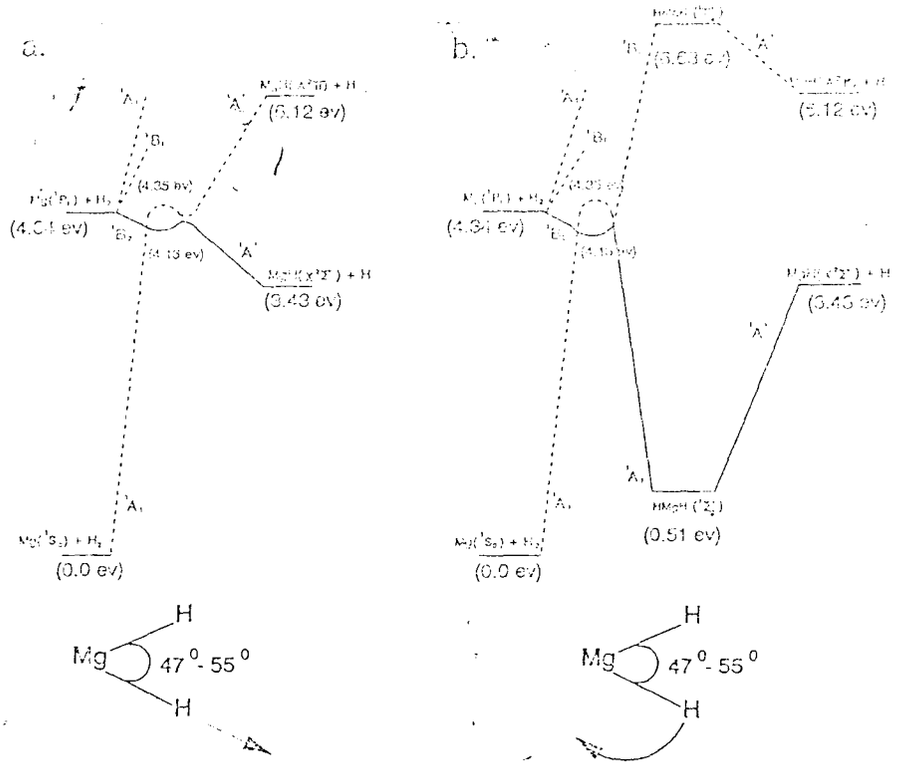

FIG. 6. (a) Reaction pathway that accounts for the previous experimental findings of MgH produced in the lower rotational states and preferentially $v''=0$. The bent intermediate decomposition follows the stretching direction of Mg–H elongation. (b) Reaction pathway that accounts for MgH produced in the higher rotational states with comparable $v''=0$ and $v''=1$ population. The intermediate decomposition passes through a linear geometry. For both pathways, the state energies relative to the $Mg(^1S_0)+H_2$ reactants are calculated with a MP4/6-31G** method. The MgH_2 intermediate near the crossing region is calculated at the bending angle of 50°.

For further conducting quasiclassical trajectory (QCT) calculation, we have applied method II to construct the dynamical PES's for the excited and ground state in the current reaction. The *ab initio* PES's were then converted to an analytic potential energy function, including 34 parameters, using a many-body expansion method.[28] Based on these parameters, a QCT program was performed and led to a bimodal rotational distribution, which is consistent with the aforementioned observation.[1–4] The QCT results confirm the reliability of our PES's computation by method II, and further lend support to the interpretation for the microscopic pathways. We will report the energy function and QCT calculation elsewhere.[29] As shown in Fig. 10, a two-dimensional ground state PES generated from the analytic potential energy function generally agrees with Fig. 4, but presents better quality than that with method I. Again, MgH may be produced via two pathways by means of the equipotential contour of the ground state Mg–H_2. One goes through the linear complex, and the other is along the coordinate of the MgH elongation. The trajectories for the MgH_2 decomposition shown in Fig. 10 are more feasible to recognize than those computed by method I. As mentioned previously, although the PES calculation near the region of the surface crossing is difficult to converge, we have compared the fitting energies with the *ab initio* values computed at the crossing region and the minimum position of the excited state in a C_{2v} geometry. The resulting satisfactory agreement between them assures the reliability of the crossing region shown in Fig. 10. The analytical potential energy function has taken into account ~400 grid points each for the excited and the ground states. The maximum deviation from the *ab initio* energies is 1.5 kcal/mol for the excited state HMgH at a bending angle 12° and 2.0 kcal/mol for the ground state HMgH at 60°. As the worse fitting regions are away from the surface crossing, the quality of QCT performance will not be affected.

D. Isotope and temperature effects

When the excited Mg atom approaches H_2 in a bent configuration, the H–H bond has to elongate to some extent before a nonadiabatic transition takes place. According to the PES calculation, the H–H distance in the MgH_2 intermediate around the crossing region reaches a value between 1.5 and 2.2 Å, much larger than the equilibrium distance 0.74 Å for H_2. When one H atom departs, the restoring force exerted directly on the other H atom may well be negligible. Similarly, in the Mg–HD reaction, HD becomes loosely bonded, when the MgHD intermediate reaches the surface crossing. Thus the D-atom removal may leave insignificant impact on the H atom. This fact accounts for the lack of isotope effect. Of course, we believe that the behavior of isotope effect is more complicated than what we may comprehend. Here we simply provide some insight from the kinematic point of

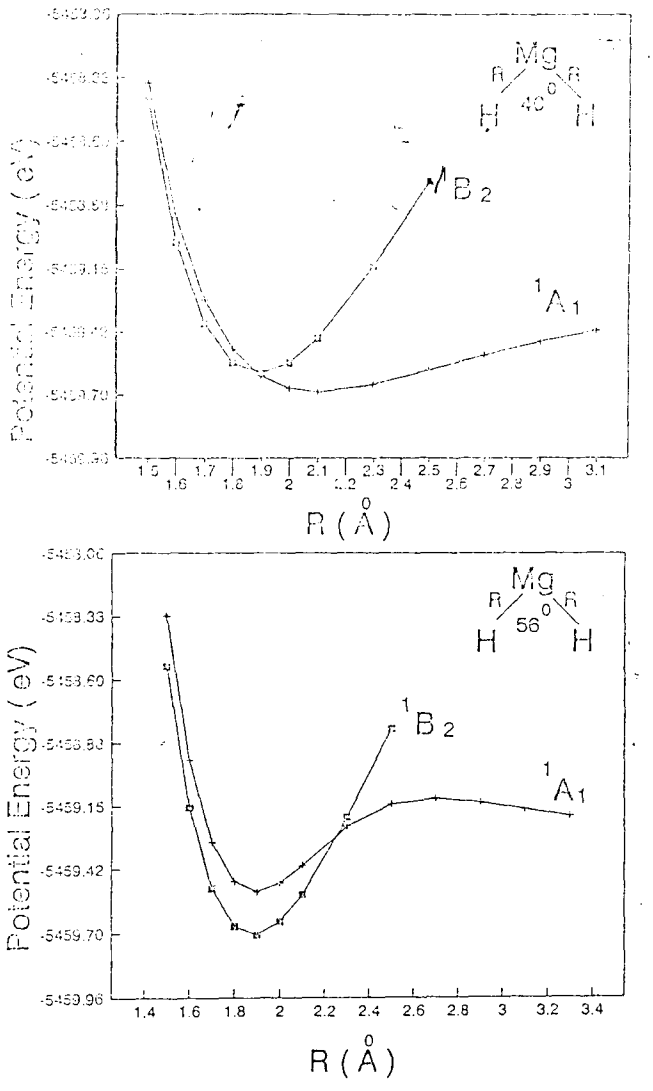

FIG. 7. The potential energies of the MgH_2 complex ($^1B_2$ and $^1A_1$) as a function of bond angle and bond length. Two cases are shown with the bond angle fixed at 40° and 56°.

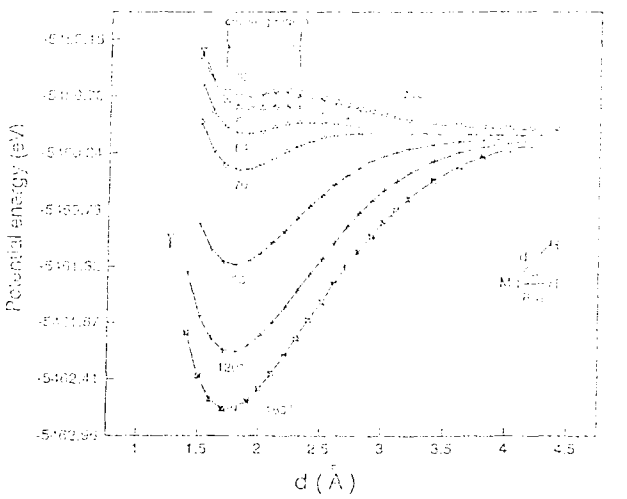

FIG. 8. The potential energies of the MgH_2 ground state as a function of bond angle and bond length, when the other bond length is fixed at the optimized distance ~1.7 Å calculated under a C_{2v} geometry. The surface crossing region is marked. The intermediate decomposition may follow two directions, Mg–H elongation or angle expansion.

a diatomic potential associated with Mg and the departing H(2) atom, while H(1) is treated as a spectator. Because Mg is much heavier than H, according to the impulsive model, the restoring force along the H(2)–Mg coordinate cannot effectively cause the rotational excitation of MgH(1). Such a prediction is consistent with the interpretation based on the *ab initio* PES for the case of weak anisotropy. The impulsive model becomes reliable in the sense that the PES results meet the required assumption.[12–16]

Nevertheless, the lack of a detailed PES information had misled the mechanism proposed for the low-N MgH distribution to stem from a direct dissociation from a linear HMgH complex.[1,4] Such a consideration is essentially made under the assumption that the linear HMgH is long-lived enough to allow for complete dissipation of the excess energy. As to the temperature effect, it may also be rationalized in terms of the PES's information. Since the rotational bimodality originates from the same intermediate in the entrance channel, which in turn proceeds a nonadiabatic transition and then decomposes through two distinct pathways, the low-N and high-N components in the MgH distribution should respond to an identical temperature dependence as observed previously.[3]

E. Impulsive model vs PES

In the light of PES's calculation, validity of the impulsive model may be examined effectively. The pathway leading to the low-N MgH product is taken as an example. In this case, one may find that the H(1)–H(2) bond becomes dissociative when the Mg–H_2 reaches the crossing region, and the bond length of the MgH(1) product is weakly varied throughout the dissociation process. Therefore, the Mg–H_2 interaction potential may well be reduced to only one term of

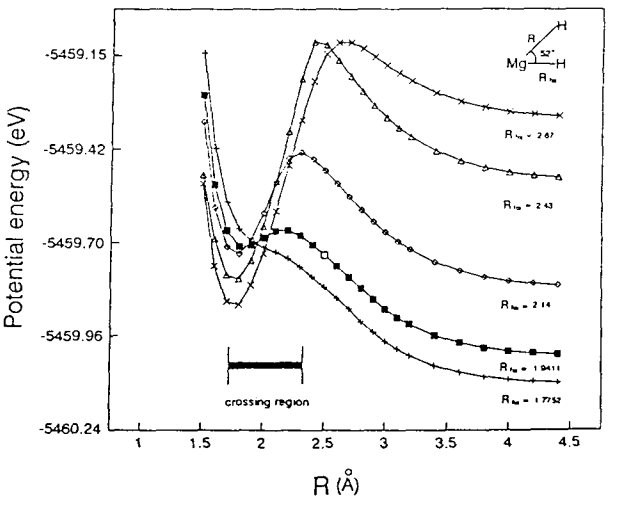

FIG. 9. The energy dependence of the MgH_2 ground state on the bond length, when the other bond length is fixed at various distances, but the bond angle is at 52°. The crossing region with the excited state is marked.

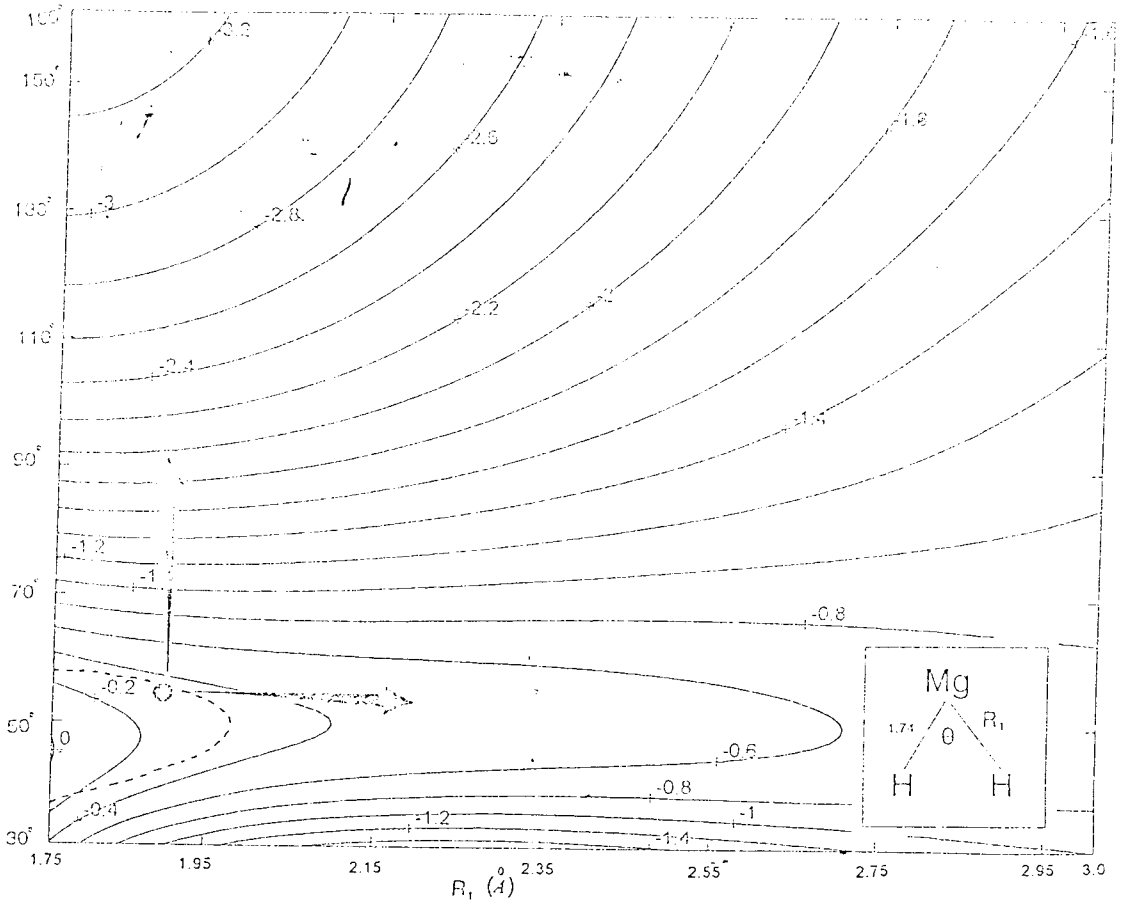

FIG. 10. Two-dimensional ground state PES generated from an analytic potential energy function. The dashed circle denotes the surface crossing region and the arrows indicate the probable pathways for the intermediate decomposition.

ergy deposited in the complex before decomposition. But the MgH_2 complex with only three vibrational modes should dissociate rapidly. The prediction by the impulsive model, which ignores the influence of the bond angle dependence, opposes the interpretation based on the PES information.

IV. CONCLUSION

By means of the PES information provided in this work, we may appropriately account for the reaction pathways for MgH produced in the $Mg(^1P_1)-H_2$ collision. As $Mg(^1P_1)$ approaches H_2 in a bent configuration, a nonadiabatic transition has to take part in the reaction to obtain MgH in the $^2\Sigma^+$ state. If the MgH_2 intermediate decomposes along the stretching coordinate of the Mg–H elongation, the resulting MgH may be produced in the low rotational states and preferentially $v''=0$, as observed experimentally. In contrast, if the intermediate decomposition passes through a linear geometry, MgH is anticipated to populate in the quantum states of rotational and vibrational excitation. The isotope and temperature effects on the MgH rotational distribution are also well explained with the calculated PES's. The impulsive model fails to interpret the current reaction, in which the same intermediate is responsible for two distinct rotational and vibrational distributions.

ACKNOWLEDGMENTS

The authors wish to thank Professor C. Witting and Dr. K. Liu for their helpful discussions. This work is supported by the National Science Council of the Republic of China under Contract No. NSC87-2119-M-002-001.

[1] W. H. Breckenridge and H. Umemoto, J. Chem. Phys. 80, 4168 (1984).
[2] W. H. Breckenridge and J. H. Wang, Chem. Phys. Lett. 137, 195 (1987).
[3] K. C. Lin and H. C. Chang, J. Chem. Phys. 90, 6151 (1989).
[4] D. K. Liu, T. L. Chin, and K. C. Lin, Phys. Rev. A 50, 4891 (1994).
[5] P. D. Kleiber, A. M. Lyyra, K. M. Sando, S. V. Zafiropulos, and W. C. Stwalley, J. Chem. Phys. 85, 5493 (1986).
[6] P. D. Kleiber, A. M. Lyyra, K. M. Sando, S. P. Heneghan, and W. C. Stwalley, Phys. Rev. Lett. 54, 2003 (1985).
[7] R. P. Blickensderfer, K. D. Jordan, N. Adams, and W. H. Breckenridge, J. Phys. Chem. 86, 1930 (1982).
[8] P. Chaquin, A. Sevin, and H. Yu, J. Phys. Chem. 89, 2813 (1985).
[9] S. Bililign and P. D. Kleiber, J. Chem. Phys. 96, 213 (1992).
[10] S. Bililign, P. D. Kleiber, W. R. Kearney, and K. M. Sando, J. Chem. Phys. 96, 218 (1992).
[11] J. G. McCaffery, J. M. Parnis, G. A. Ozin, and W. H. Breckenridge, J. Chem. Phys. 82, 4945 (1985).
[12] G. E. Busch and K. Wilson, J. Chem. Phys. 56, 3626 (1972).
[13] D. S. Perry and J. C. Polanyi, Chem. Phys. 12, 37 (1976).
[14] H. B. Levene and J. J. Valentini, J. Chem. Phys. 87, 2594 (1987).
[15] R. Schinke, Comments At. Mol. Phys. 23, 15 (1989).
[16] R. Schinke, *Photodissociation Dynamics* (Cambridge University Press, Cambridge, 1993).
[17] P. Andresen and R. Shinke, in *Molecular Photodissociation Dynamics*,

edited by M. N. R. Ashfold and J. E. Baggott (Royal Society of Chemistry, London, 1987).
[23] A. Hodgson, J. P. Simons, M. N. R. Ashfold, J. N. Bagley, and R. N. Dixon, Chem. Phys. Lett. 107, 1 (1984).
[24] M. J. Frisch, M. Head-Gordon, G. W. Trucks, J. B. Foresman, H. B. Schlegel, K. Raghavachari, M. A. Robb, J. S. Binkley, C. Gonzalez, D. J. DeFrees, D. J. Fox, R. A. Whiteside, R. Seeger, C. F. Melius, J. Baker, R. L. Martin, L. R. Kahn, J. J. P. Stewart, S. Topiol, and J. A. Pople, GAUSSIAN 92, Gaussian Inc., Pittsburgh, Pennsylvania, 1992.
[25] M. A. Khan, Proc. Phys. Soc. London 89, 203 (1962).
[26] R. Ahlrichs, F. Keil, H. Lischka, W. Kutzelnigg, and V. Staemmler, J. Chem. Phys. 63, 455 (1975).
[27] M. M. Francl, W. J. Pietro, W. J. Hehre, J. S. Binkley, M. S. Gordon, D. J. DeFrees, and J. A. Pople, J. Chem. Phys. 77, 3654 (1982).
[28] M. F. Guest and S. Wilson, Chem. Phys. Lett. 72, 49 (1980).
[29] B. O. Roos, P. R. Taylor, and P. E. M. Siegbahn, Chem. Phys. 48, 157 (1980).
[30] G. Herzberg, *Molecular Spectra and Structure* (Van Nostrand, New York, 1950), Vol. I.
[31] R. S. Mulliken, J. Chem. Phys. 23, 1833 (1955).
[32] J. R. Hoyer and R. Schinke, J. Phys. Chem. 97, 3463 (1993).
[33] J. N. Murrell, S. Carter, S. C. Farantos, P. Huxley, and A. J. C. Varandas, *Molecular Potential Energy Functions* (Wiley, New York, 1984).
[34] Y. R. Ou and K. C. Liu (unpublished).

[illegible]

[illegible]*

[illegible] Chemistry, National Taiwan University, Taipei 1, Taiwan 106, and
[illegible] Molecular and Molecular Science, Academia Sinica, Taipei, Taiwan 106, Republic of China

A laser-enhanced two-step laser-enhanced ionization (LEI) technique is potentially useful in monitoring a spatially resolved [illegible] in atmospheric air-acetylene flame. As a complement to other optical methods, LEI detection shares the advantages of relatively high sensitivity and the capability of achieving high spatial resolution, confined to the dual-beam intersection [illegible] mm). A theoretical model was developed to precisely extract the temperature information from the obtained two-step LEI signal. The physical parameters required in the experiment include simply the relative values of the LEI signals, associated with the fine-structure doublets of a selected thermometric species, and their corresponding laser energies. The subsequent treatment is also convenient without the need to know the absolute energy of the incident laser beam and to accurately calibrate the detection system. Al and Ga were selected as the thermometric species. The resultant radial and axial temperature mappings are consistent with each other and are also comparable with those reported by other optical methods.

Index Headings: Laser-enhanced ionization; Flame temperature determination.

INTRODUCTION

Flame temperature measurement has been an important subject in the field of combustion chemistry. Any chemical kinetics, thermal equilibrium, ionization, excitation, and other physical behavior in an analytical flame may be significantly characterized by its environmental temperature. Therefore, accurately diagnosing the temperature provides a basis for further understanding of these chemical and physical events and is also conducive to optimizing the combustion parameters in a flame.[1-3] For monitoring the flame temperature, a spectroscopic method provides a nonintrusive measurement, having the advantage of avoiding interference from combustion components. Two-line emission or absorption and line-reversal methods are conventionally used as the tools.[1-3] Laser-based techniques such as laser-induced fluorescence (LIF),[4-6] coherent anti-Stokes Raman scattering (CARS),[3,7] Rayleigh scattering, and degenerate four-wave mixing (DFWM) are commonly employed.[8-10] Most of these methods rely on the assumption of a local thermal equilibrium, in which the flame temperature is represented in terms of electronic, vibrational, rotational, and translational behavior of the seeded thermometric species.

The CARS technique is capable of achieving a high spatial and temporal resolution for a temperature mapping. However, it is limited by weak sensitivity, so that high number density of the thermometric species is required.[7] The LIF method offers better detection sensitivity, but sometimes suffers from collisional quenching and post-filter effects. Thus, a more complicated but careful manipulation is needed to extract the temperature information from the obtained signal. The DFWM method has been recently developed to measure rotational temperature. With the capability of detecting trace levels without suffering from interference from a flame background, this technique proves to be potentially useful for probing high spatial resolution of the temperature. As applied to thermometry, however, this method requires a critical understanding of the dependence of the scattering cross section on the rotational quantum number. Another problem, for instance, encountered by a broad-band DFWM approach arises from the narrowness of the laser spectral band. Thus only a few rotational lines can be covered in one laser shot, and the corresponding temperature may possibly include a large error.[8] As a complement to these optical methods, in this work, we demonstrate an alternative approach based on a two-step laser-enhanced ionization (LEI) technique. This kind of LEI detection proves to be capable of mapping flame temperatures with high spatial resolution and sensitivity.

Laser-enhanced ionization spectroscopy in flames has been successfully developed to detect trace metal concentrations at the sub-pg/mL level in aqueous solution with extremely high sensitivity and selectivity.[11-16] In addition, applications may include such tasks as measurement of the number density of free atoms released and, in turn, the atomization efficiency,[17] monitoring of ion lifetime,[18] determination of ion diffusion and mobility coefficients,[19,20] and resolution of spectral structures of atoms, molecules, and radicals.[21] The LEI technique can also be interfaced to flow injection to reduce matrix interference effects[22,23] and serve as a chromatographic detector.[24,25] As reported previously, by measuring ion mobility and diffusion coefficients of a thermometric species, one may determine the flame temperature on the basis of the Einstein relation.[20] The advantage of the LEI method lies in its capabilities of achieving high spatial resolution and avoiding optical interference from scattered radiation and flame background radiation. Nevertheless, one should assume that the size of the electrode as the ion collector is negligible and the electric field applied between them homogeneous. A precise measurement of ion diffusion and mobility coefficients is not trivial. An error propagation may lead to a large systematic error. Instead of using the Einstein relation, we have re-

Received 30 May 1997; accepted 27 August 1997.
* Author to whom correspondence should be sent.

0003-7028/98/5202-0187$2.00/0

cently developed a model to relate the measured LEI signals to the corresponding Boltzmann populations of the fine-structure doublets of the thermometric species, from which the electronic excitation temperature may be derived.[26] The feasibility and accuracy of the LEI temperature detection are found to be comparable to those of other optical methods. However, the temperature thus obtained is restricted to a spatial average along the laser beam directed through the slot burner.

In this work, we use stepwise excitation to enhance the LEI signal intensity, improving the detection sensitivity by up to two orders of magnitude. In addition, the configuration of the dual-laser beams is arranged in such a way that one beam intersects perpendicularly with the other one inside the flame. The temperature results for the interaction regime are confined to a very limited size. In this manner, the LEI method shares the advantages of extremely high sensitivity and capability of achieving a spatially resolved temperature, as in LIF and DFWM. We also developed a theoretical model, based on previous work,[26] to extract the temperature information from the measured two-step LEI signal. We measured radial and axial temperature profiles, with Al and Ga as the thermometric species, to demonstrate the reliability of this technique. A comparison with other optical methods will be discussed.

EXPERIMENTAL

Flame Burner. The experimental apparatus of a two-step LEI has been illustrated previously,[11,15,16,26] so only a brief description is given below. We performed the LEI experiment, as shown in Fig. 1, by using a commercial burner assembly (Perkin-Elmer) with a 100 mm × 0.5 mm slot burner head, coupled with an interlocked gas control system by which acetylene (0.8 L/min) and air (13 L/min) were premixed prior to reaching the burner head.

Reagent. Al and Ga chloride salt were used as the reagents. Each aqueous salt solution was nebulized at a flow rate of 4.5 mL/min into the flame. The linearity of concentration dependence of the LEI signal has been carefully checked. Thus, the concentrations of 150 and 50 ppm (μg/mL) of Al and Ga salt solutions, which lay [illegible] the experiment of temperature determination.

[illegible] System. In this work, two tunable dye lasers (Spectra-Physics PDL-2A and PDL-3), each pumped by a pulsed Nd:YAG lasers (Spectra-Physics, DCR-2A and GCR-3), were used as radiation sources. One dye laser was operated so that the beam propagated horizontally through the flame and [illegible] perpendicularly with the other one. The configuration is shown in Fig. 1b. The intersection position was varied smoothly by changing lateral slide with a set of micrometer-driven translational stage, equipped with [illegible] to the burner. The height from the burner top was adjusted from 2.5 ± 0.5 to 12.5 ± 0.5 mm. The two beams were chopped temporally and [illegible] Pulse. The individual beam was [illegible] mm in diameter to [illegible] the [illegible] the vertical [illegible] was minimized, so that [illegible] of sample atoms caused by light scattering could be neglected.[27]

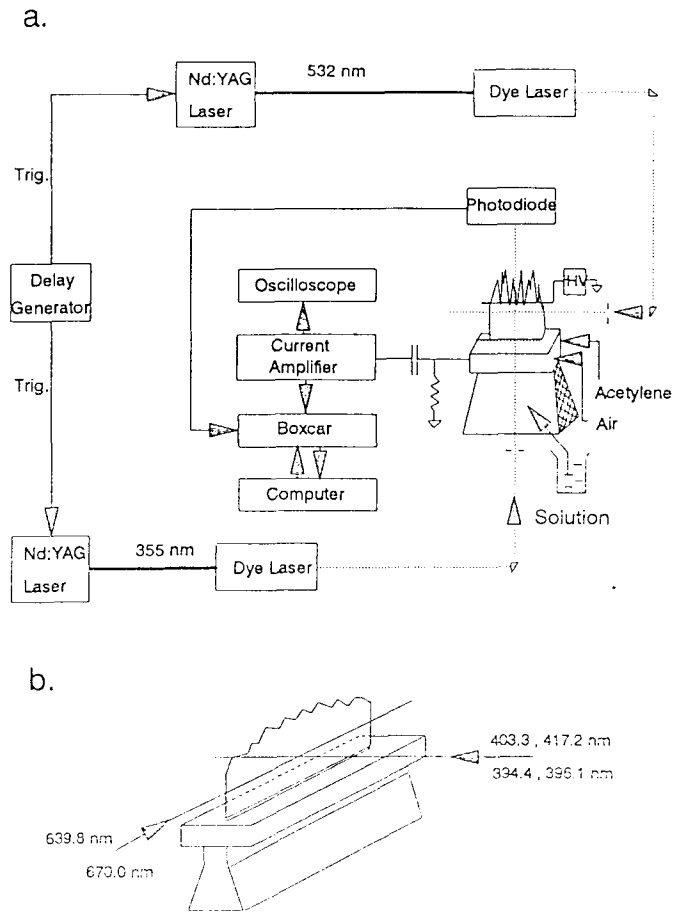

FIG. 1. (a) Schematic diagram of the experimental setup for the two-step LEI detection. (b) The configuration of dual laser beams directed towards the flame.

Two-Step LEI Detection System. The energy schemes of the two-step LEI process for Al and Ga are shown in Fig. 2. For the case of Al, the first laser was scanned over the wavelength range of 393–397 nm to select the atomic transitions from the fine-structure doublets to the $4^2S_{1/2}$ state, while the second laser was fixed at [illegible] nm [illegible] eV, for the case of Ga, the wavelength range of the first laser was scanned over 302–418 nm, while the second laser was fixed at 639.8 nm. As the second photon laser was resonant with the $^2S_{1/2}$ [illegible] stepwise excited atoms could be subsequently collisionally ionized. The resulting LEI ions were collected with a stainless steel cylinder probe of [illegible] biased at −100 V and separated [illegible] mm from the flame. [illegible] the flame, about 6 mm off the axis of the burner. The ion current in this work proved to be comparable to that obtained with the chevron [illegible] The [illegible] was fixed at the center of the flame [illegible] was [illegible] Fig. 1b. [illegible] was [illegible] 4125 Å, and [illegible] Fig. 2.

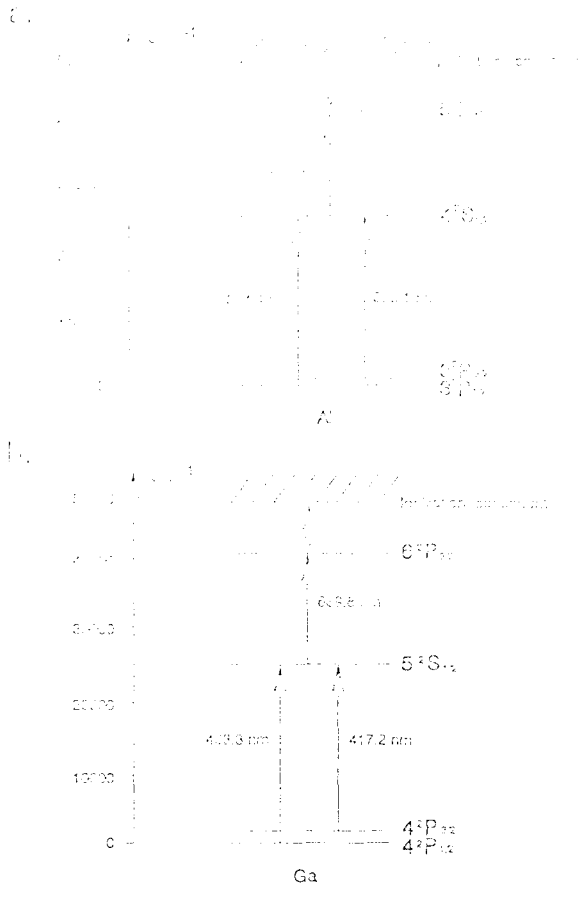

FIG. 2. Partial energy diagrams for the Al and Ga atoms.

an oscilloscope (Tektronix, Model 2445) or stored in a microcomputer for later data treatment. The corresponding laser energy for the first-step excitation was monitored simultaneously with either a photodiode (Hamamasu, s2386) or an energy meter (Scientech 36-0001).

THEORETICAL MODELING

The theoretical modeling for the two-step LEI detection approach is based on our previous work with one-step LEI.[26] The essence of the model relies on the association of the temperature with a Boltzmann population difference between the ground and the excited fine-structure doublets of a selected species. The relationship between the observed ion signal and the state population affects the reliability and precision of the estimated temperature.

One-Step LEI. The energy schematic diagrams of single-step and two-step LEI are displayed in Fig. 3. The populations in the ground and excited fine-structure state, l and l', are excited alternatively to an intermediate state u, and then ionized via the collisional process. For the two-step LEI scheme, an additional photon promotes the population from the u state to a higher h state. In the LEI scheme, Omenetto et al.[13] and Travis[28] suggest that the ion yield is proportional to the product of the steady-state population density, n_u, of the excited state, and its collisional ionization rate coefficient, K_{ui}. Within the limit of the two-level approximation and with the assumption of

FIG. 3. Energy diagrams employed to the method of (a) one-step LEI and (b) two-step LEI.

a broad-band laser, the population density for n_u and n_l may be derived as

$$n_u = n_t g_u I_\lambda / (g_u + g_l) I_\lambda + I_s), \tag{1}$$

$$n_l = n_t ((g_u + g_l) I_\lambda + I_s) / (g_u + g_l)(I_\lambda + I_s) \tag{2}$$

where n_t denotes the total population density, equal to $n_u + n_l$; g_u and g_l are the statistical weight for the u and l state; I_λ is the spectral irradiance; and I_s is its saturation parameter. If a relatively weak laser intensity, $I_\lambda \ll I_s$, is assumed, and n_l is close to its thermal population density n_l^{th}, then n_u can be approximated by

$$n_u \approx n_l^{th} (g_u/g_l) I_\lambda \lambda_{ul}^5 A_{ul} \tau_u / (8\pi hc^2) \tag{3}$$

where τ_u is the lifetime of the upper state u; A_{ul}, the Einstein spontaneous emission coefficient from the u to l state; λ_{ul}, the emission wavelength from the u to l state; c, the light speed; and h, Planck's constant. If a fast collision redistribution among excited states lying between the state u and the continuum state i is assumed, then the ionization rate coefficient K_{ui}, due to collision, for the state u may be given as[13]

$$K_{ui} = \bar{\nu} \sigma_u n_i \exp[-(E_i - E_u)/kT] \tag{4}$$

where σ_u is the cross section for the colliding process; $\bar{\nu}$, the relative average velocity between the atom and the collider in the flame; n_i, the number density of the collision partner; T, the flame temperature; and E_i and E_u, the energy of the continuum and the upper state, respectively. Thus the single-step LEI signal S_{lu} from the ground fine-structure state l can be described as

$$S_{lu} \propto n_l^{th} (g_u/g_l) I_\lambda \lambda_{ul}^5 A_{ul} \exp[-(E_i - E_u)/kT]. \tag{5}$$

Note that the values of $\bar{\nu}$, σ_u, τ_u, and n_i for the single-step LEI scheme initiated from either the l or l' state are the same; thus these parameters are omitted in Eq. 5 when comparing the LEI signals between S_{lu} and $S_{l'u}$.

Two-Step LEI. The ion enhancement induced by a two-step LEI scheme is strongly affected by the second-step excitation. The explicit formula is expressed as[15]

$$S_{lh}(\text{TLEI}) = \frac{\lambda_{uh}^2 A_{hu} I_{uh} k_{hi}}{2\pi \Delta\omega_{uh} k_{ui}} S_{lu}(\text{SLEI}). \tag{6}$$

The ion enhancement of two-step LEI (TLEI) over single-step LEI (SLEI) may be attributed to such factors as second-step transition probability, laser intensity, colli-

sional ionization rate coefficients, and transition linewidth, which is associated with the effective lifetime of the states involved in the transition. Equation 6, ignoring the possibility of atom depletion during the laser pulse, is equivalent to equation 36 given by Axner et al.[29] The atom depletion effect may become negligible by an appropriate selection of the upper state *h*, so that the inverse of collisional ionization rate from this state is larger than the laser pulse duration.[15]

Provided that the laser energy and wavelength for the second-step excitation are fixed, the enhanced factor becomes constant. Analogously to Eq. 5, therefore, the TLEI signal can be expressed as

$$S_{lh}(\mathrm{TLEI}) \propto F n_l^{\mathrm{th}}(g_u/g_l) I_\lambda \lambda_{ul}^5 A_{ul} \exp[-(E_l - E_u)/kT]. \qquad (7)$$

The proportional constant F is the same for both TLEI signals associated with the l and l' states. The ratio of the thermal population density, n_l^{th} and $n_{l'}^{\mathrm{th}}$, for the ground and the excited fine-structure doublets follows the Boltzmann distribution. That is,

$$n_l^{\mathrm{th}}/n_{l'}^{\mathrm{th}} = (g_l/g_{l'})\exp[-(E_l - E_{l'})/kT]. \qquad (8)$$

Asuming that the laser energy for the first-step excitation is weak, using the relations in Eqs. 7 and 8, we can derive the ratio of two-step LEI signals associated with the ground and the excited fine-structure doublets as

$$S_{lh}(\mathrm{TLEI})/S_{l'h}(\mathrm{TLEI}) = (I_\lambda/I'_\lambda)(\lambda_{ul}^5/\lambda_{ul'}^5)(A_{ul}/A_{ul'}) \exp[(E_{l'} - E_l)/kT]. \qquad (9)$$

This equation is further rearranged to give an explicit, practical relation for the temperature measurement in this work as

$$T = (E_{l'} - E_l)/(kQ), \qquad (10)$$

$$Q = \ln(S_{lh} I'_\lambda \lambda_{ul'}^5 A_{ul'}/S_{l'h} I_\lambda \lambda_{ul}^5 A_{ul}). \qquad (11)$$

Given the spontaneous transition propabilities and the corresponding wavelengths for the pertinent atomic transitions, by measuring the LEI signal, one may determine the flame temperature using Eqs. 10 and 11. For an alternative excitation scheme, $l \rightarrow u$ and $l' \rightarrow u'$, in which the intermediate states u and u' are different, an analogous equation may also be derived. However, additional parameters involved may reduce the accuracy of the determined temperature.

RESULTS AND DISCUSSION

[illegible] are described [illegible] by [illegible] *LEI Spectra and Data Treatment*. In the case of Al, the first laser was scanned across the transitions of [illegible] ← [illegible], while the second laser was fixed at 670.0 nm. The resulting two-step LEI signal is shown in Fig. 4. If the laser at 670.0 nm was blocked, the single-step LEI was taken under otherwise identical condition. As shown in Fig. 4, one can hardly observe any single-step LEI signal for the Al atom. We could not detect any signal either as a result of irradiation of the second laser alone at 670.0 nm. The lack of a detectable single-step LEI signal arises from the [illegible] is attributed to the fact that the detected [illegible] of the species is restricted to a very small volume. The beam

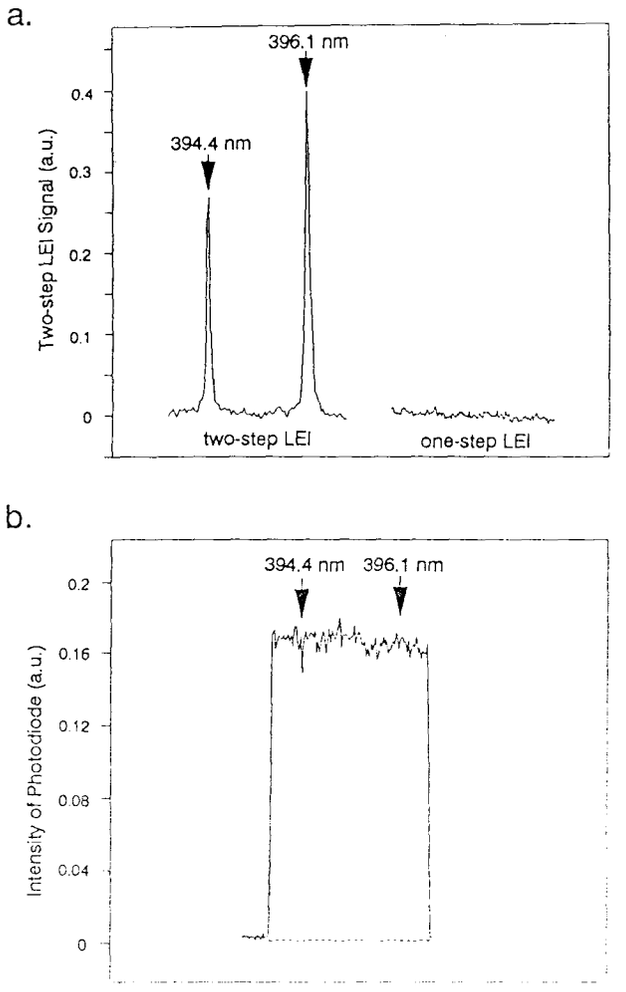

FIG. 4. (a) Two-step and one-step LEI spectra of 150 ppm Al. The former spectrum was obtained with irradiation of dual lasers simultaneously, while the latter was obtained without irradiation of the second laser at 670.0 nm. (b) The corresponding laser energy for the first-step excitation.

arrangement for the first laser is guided perpendicularly to the axis of the burner slot, unlike the conventional LEI alignment with the laser directed along the flame burner. The current LEI detection of Al provides a very [illegible] and steady ion background, [illegible] by the [illegible] laser ionization process alone. In this sense, the [illegible] LEI apparatus is operated like a [illegible] rather than a differential measurement [illegible] the measured signal-to-noise ratio is greatly [illegible]. In addition, the measured LEI signal [illegible] partially overlapped region between [illegible] derived temperature [illegible]

For the [illegible] They are (1) [illegible] ratio of [illegible] and (2) the ratio of [illegible] the respective first-step excitation [illegible] The validity of [illegible] energy separation of the fine-structure doublets [illegible]

responding energies at these two transition wavelengths were almost the same (Fig. 4). The laser energy was measured with a photodiode, since there was no need to measure the absolute value. Whenever it is necessary, the exact energy may be readily measured with an energy meter instead. In th[is] work, we kept the energy of the second laser at 150 [μJ] which is linear in the region, as well. In fact, it is u[n]necessary, because Eqs. 10 and 11 are applicable to both conditions of optical saturation and unsaturation for the second-step laser.

Temperature Profiles. Given the slopes, S_{III}/I_X and S_{I+II}/I_X, the corresponding excitation wavelengths, and the spontaneous emission coefficients, the temperature may be evaluated. The related parameters are listed in Table I. The beam direction of the first laser was moved successively along the side of the flame; thereby the radial temperature profile, at 10 mm above the burner head, was obtained (Fig. 6a). The error bars were estimated for five replicates. The temperature varied from 2400 to 2550 K. The values in the central region appear to be 150 K higher than those near the edge. A cooler flame in the edge is readily interpreted as arising from intrusion of the ambient air. We also measured the axial-position dependence of the flame temperature by adjusting the height from 2.5 mm to 12.5 mm above the burner head. The result is shown in Fig. 6b, in which the radial position at 0 mm was measured. It is found that the temperature declines slightly from 2550 to 2500 K as the height is increased. The measured temperature profiles for both axial and radial distributions seem to be very steady without any dramatic changes.

Spatial Resolution. In this work, the spatial resolution of the flame temperature was confined within 1 mm × 1 mm, depending on the aperture through which the unfocused laser beam was directed. In theory, the spatial resolution may be improved to the micrometer level, if a focused beam is used for the first-step excitation. The slight difference in beam waists caused by different transition wavelengths for the doublets will not introduce much error in the evaluation of the S_{III}/I_X value, if one is careful to measure the laser energy at the interactive position. The major problem to avoid arise[s] from the fact that the focused beam of the first laser easily results in optical saturation, which will not meet the model conditions.

Temperature Determination by Ga Species. The energy difference between the fine-structure doublets of Al is 112 cm^{-1}. The small energy separation does not allow for very accurate temperature determination. Therefore, we select the other thermometric species of Ga, with an energy separation of 827 cm^{-1} between the doublets, to

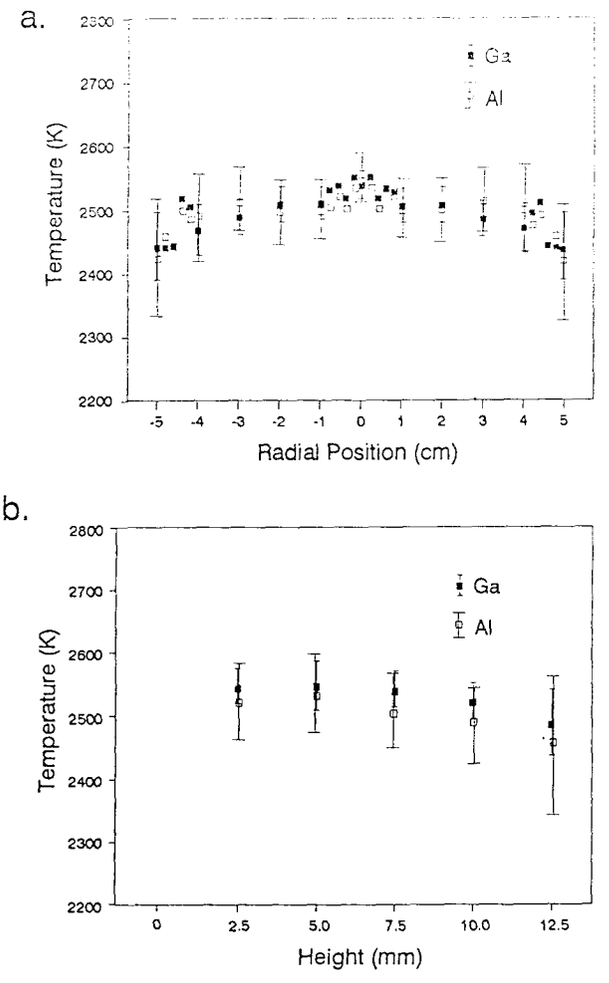

FIG. 6. (a) Radial temperature profile, measured at a height 10 mm from the burner top. (b) Axial temperature profile, measured at the central burner.

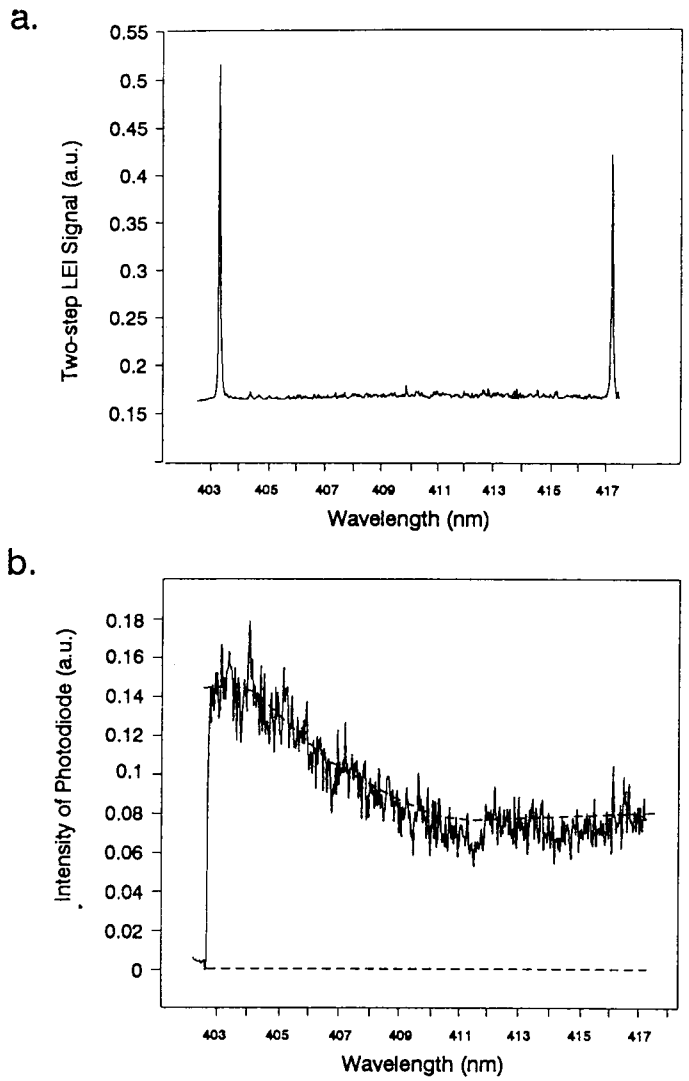

FIG. 7. (a) Two-step LEI spectra of 50 ppm Ga, of which one laser is scanned across the atomic transition $5^2S_{1/2} \leftarrow 4^2P_{1/2,3/2}$ while the other laser is fixed at 639.8 nm. (b) The corresponding laser energy for the first-step excitation, detected with a photodiode.

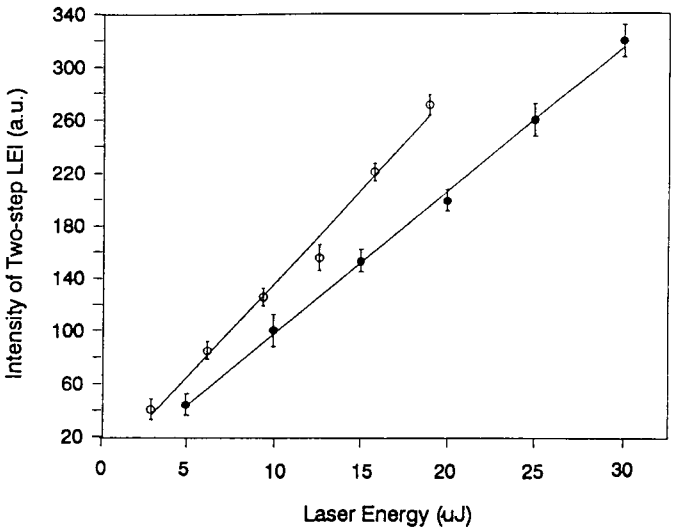

FIG. 8. Laser energy dependence of two-step LEI signals, associated with the atomic transitions at 403 nm (●) and 417 nm (○), respectively, from the ground and the excited fine-structure doublets of the Ga atom. The concentration of Ga was 50 ppm. The second laser at 639.8 nm was fixed at 120 μJ.

confirm reliability with the two-step LEI model. The wavelength of the first laser was scanned across the atomic transitions $5^2S_{1/2} \leftarrow 4^2P_{1/2,3/2}$, while the second laser was fixed at 639.8 nm. The resultant LEI signal is shown in Fig. 7, which was probed in the central position, 10 mm above the burner head. The figure also displays the corresponding energy of the first laser, as measured with a photodiode. Its radiant sensitivity at a wavelength of 417 nm was reported to be 7% larger than that at 403.3 nm. The corrected energy dependence of the two-step LEI signals, initiated from either the $4^2P_{1/2}$ or the $4^2P_{3/2}$ state, exhibits a relation of linear proportion, as shown in Fig. 8. The condition of the second laser at 639.8 nm was kept at 120 μJ, which was controlled to be unsaturated, although it was not necessary. Substituting the measured slopes and the relavent parameters into Eqs. 10 and 11, one may determine the spatially resolved flame temperature. By analogy with the Al case, the flame temperature was measured axially and radially, as shown in Fig. 6. Each error bar was estimated for five replicates. The distribution of the temperature profile is consistent with the case obtained with Al.

The temperature uncertainty ΔT can be evaluated according to Eq. 12:

$$\frac{\Delta T}{T} = \frac{kT}{E_{l'} - E_l}\sqrt{\left(\frac{\Delta S}{S}\right)^2 + \left(\frac{\Delta I}{I}\right)^2} \qquad (12)$$

where k is the Boltzmann constant; S and I denote the measured LEI signal and the corresponding laser energy. ΔT is reciprocally proportional to the energy difference $E_{l'} - E_l$. The use of Ga as the thermometric species to replace Al may theoretically improve the temperature precision by a factor of 8. While considering the standard deviations of the measured LEI signal and the laser energy, we find that Ga yields a temperature precision two times better than Al (Fig. 6).

Comparison with Other Optical Methods. *Advantages of Two-step LEI.* As compared with the old versions of LEI temperature detection,[20,26] this study has several advantages. First, the new method provides a feasible and convenient way to carry out the experiment. The temperature determination relies on a straightforward measurement of the relative values of the LEI signals and the corresponding excitation energy associated with the fine-structure doublets. There is no need to calibrate the detection system and to monitor the absolute energy of the incident laser. Second, this work is capable of achieving a high spatial resolution. Third, a two-step LEI is used instead, improving markedly the sensitivity to the species detection. In the cases of Ga and Al, for instance, the ion enhancement of two-step LEI over single-step LEI was measured herein to be a factor of 30 and 600, respectively, as the configurations of two beams were changed to propagate in the opposite direction along the burner slot. The only restriction for this version is to assume validity of the steady-state approximation for the first-step intermediate state and a local thermal equilibrium in the flame. In the LEI scheme, a weak excitation rate is

applied, and subsequently the excited population is removed rapidly due to a relatively large ionization rate. This observation suggests that the steady-state approximation should be applicable to the system.[13,28,30] The assumption of a thermally equilibrated flame is the premise for those detection methods applying Boltzmann distribution.

Temperature by Other Optical Methods. To justify the reliability of our LEI measurement, we compared the measured temperature in an atmospheric air/acetylene flame with various optical methods. These methods include atomic absorption (AA),[31,32] atomic emission (AE),[31,33] atomic fluorescence (AF),[34–36] and the LEI measurement[26] reported previously. Although different ratios of air to acetylene have been adopted, one finds that the resultant temperatures tend to decrease in a fuel-rich flame. Using the AF method, for instance, Haraguchi and Winefordner reported a temperature of 2400 K with an air/fuel ratio of 7.6:1.04 at a 3 mm height above the burner head.[36] In terms of AA measurement, Browner and Winefordner gave a value of 2450 K with the ratio of 9.5:1.3 at a 4.5 mm height.[32] With the AE method, Kirkbright et al. obtained a result of 2420 K with the ratio of 10.0:1.35 at the 4.5 mm height.[33] With the use of AA coupled to fiber-optics detection, Wang et al. reported a lower temperature of 1910–2230 K at a height range of 5–30 mm in an even more fuel-rich flame, into which the flow rates of air and acetylene were 6.7 and 1.7 L/min.[37] The latter discrepancy may arise from the presence of more carbon-containing radicals; incomplete reaction may lower the resulting temperature. In contrast, the previous LEI measurement exhibited a slightly higher temperature of 2504–2521 K in a fuel-leaner flame, composed of an air/fuel ratio of 12.5:0.5 at 7.5 mm from the burner top.[26] The combustion thus obtained was more complete. Fernandez and Bastiaans have demonstrated the stoichiometry effect on the flame temperature in the central portion, 11 cm above the top of a premixed Meker-type burner.[38] They found that the temperature tended to increase to a maximum with an increase in the ratio of air to acetylene. The tendency is essentially consistent with the stoichiometry dependence found in a rectangular burner.

Radial and Axial Temperature Profiles. The present work yields a spatially resolved temperature, which greatly reduces the interference of thermal gradients and is not limited to observation of an averaged temperature along the laser-beam path. The temperatures 2550 and 2440 K were measured in the central and the edge regions, respectively. The radial distribution is roughly symmetric. The average temperature, as evaluated by summing each point-temperature along the axis of the burner slot, is consistent with that determined by old LEI method.[26] The lower temperature in the edge found by Fernandez and Bastiaans was in a cylindrical flame,[38] and that detected by Wang et al. was in a slot burner.[37] The entrainment of external air renders the flame subject to change in local stoichiometry, which decreases the temperature. The precision of temperature evaluated in the edge appears to be poor relative to the central portion, since flame instability reduces the signal-to-noise ratio. In this work, the axial flame distribution reveals that the temperature decreases slightly with height from the burner top. The tendency is consistent with the reports by Kirkbright et al. with a home-made slot burner,[39] and by Eckbreth using the CARS technique to probe a laminar propane diffusion flame.[40] In contrast, Wang et al. showed an opposite tendency in a very fuel-rich flame.[37]

RID versus LEI. In contrast to our excitation temperature measurement, Winefordner and co-workers recently determined a spatially resolved OH rotational temperature using indium-based resonance ionization detection (RID).[41,42] The RID technique is similar to the two-step LEI detection as described herein. However, the first-step population excitation in the RID detection is achieved through two mechanisms, collision-induced energy transfer and fluorescence capture.[41] The ionization detector thus has the advantages of the LEI method, including a relatively large solid angle of signal collection, a near-unity quantum efficiency, and the minimization of optical interference. The application of RID detection to the OH rotational temperature did improve the detection sensitivity and selectivity.[42] However, the following restriction seems to be imposed on the RID method; the rates of collisional energy transfer and the excitation transition probabilities induced by fluorescence capture are assumed to be independent of the flame species and the rotational quantum states of the OH radical. The RID temperature may then be derived, on the basis of theoretical modeling that is well developed for the fluorescence or emission methods. The above assumption complicates the RID method. The complexity of such indirect processes involved as the first-step excitation in the RID scheme might be the factor leading to an unexpectedly higher temperature occurring in the flame edge.[42] It might also explain, alternatively, the appearance of a relatively poor precision as compared with that for the LIF method.

CONCLUSION

The two-step LEI method has been shown to be potentially useful in measuring spatially resolved excitation temperatures in an atmospheric air/acetylene flame. Given the ratio of two-step LEI signal and its corresponding laser energy associated with the fine-structure doublets of the species selected, the flame temperature may be determined. This approach provides a convenient and accurate measurement without the need to know the absolute beam energy and to calibrate the detection system. The accuracy and precision for the measured temperature profiles in terms of Al and Ga species are comparable with those by other optical methods.

ACKNOWLEDGMENT

This work was financially supported by the National Science Council of the Republic of China under Contract No. NSC86-2113-M002-038.

1. A. G. Gaydon and H. G. Wolfhand, *Flames: Their Structure, Radiation and Temperature* (Chapman and Hall, London, 1979), 4th ed.
2. C. Th. J. Alkemade, T. Hollander, W. Snelleman, and P. J. Th. Zeegers, *Metal Vapors in Flames* (Pergamon Press, New York, 1982).
3. A. C. Eckbreth, *Laser Diagnostics for Combustion Temperature and Species* (Abacus Press, Cambridge, 1988).
4. J. D. Bradshaw, N. Omenetto, G. Zizak, J. N. Bower, and J. D. Winefordner, Appl. Opt. **19,** 2709 (1980).
5. R. G. Joklik, Combust. Sci. and Tech. **87,** 109 (1992).

6. N. Omenetto, R. Browner, J. D. Winefordner, G. Rossi, and P. Benetti, Anal. Chem. **44,** 1683 (1972).
7. D. R. Crosley, *Laser Probes for Combustion Chemistry,* ACS Symp. Ser. No. 134 (American Chemical Society, Washington, D.C., 1980).
8. P. Ewart, Ber. Bunsenges. Phys. Chem. **97,** 1625 (1993).
9. T. Dreier and D. J. Rakestraw, Opt. Lett. **15,** 72 (1990).
10. D. Kupiszewska and B. Whitaker, J. Chem. Soc. Faraday Trans. **89,** 2951 (1993).
11. J. C. Travis, G. C. Turk, and R. B. Green, Anal. Chem. **54,** 1006A (1982).
12. O. Axner, I. Lindgren, L. Magnusson, and H. Rubinsztein-Dunlop, Anal. Chem. **57,** 773 (1985).
13. N. Omenetto, Th. Berthoud, P. Cavalli, and G. Rossi, Anal. Chem. **57,** 1256 (1985).
14. C. A. van Jijk, F. M. Curran, K. C. Lin, and S. R. Crouch, Anal. Chem. **53,** 1275 (1981).
15. K. D. Su and K. C. Lin, Appl. Spectrosc. **48,** 241 (1994).
16. G. C. Turk, Anal. Chem. **53,** 1187 (1981).
17. K. D. Su, K. C. Lin, and W. T. Luh, Appl. Spectrosc. **42,** 1370 (1992).
18. G. C. Turk and N. Omenetto, Appl. Spectrosc. **40,** 1085 (1986).
19. E. G. Mallard and K. C. Smyth, Comb. Flame **44,** 61 (1982).
20. K. C. Lin, P. M. Hunt, and S. R. Crouch, Chem. Phys. Lett. **90,** 111 (1982).
21. T. A. Cool and P. J. H. Tjossem, in *Gas-Phase Chemiluminescence and Chemi-ionization,* A. Fontijn, Ed. (Elsevier Science Publishers, Amsterdam, 1985), pp. 105–116.
22. S. C. Wang and K. C. Lin, Anal. Chem. **66,** 2180 (1994).
23. S. C. Wang and K. C. Lin, Analyst **120,** 2593 (1995).
24. T. Berglind, S. Nillson, and H. Rubinstein-Dunlop, Phys. Scripta **36,** 246 (1987).
25. K. S. Epler, T. C. O'Haver, G. C. Turk, and W. A. MacCreham, Anal. Chem. **60,** 2062 (1988).
26. K. D. Su, C. Y. Chen, K. C. Lin, and W. T. Luh, Appl. Spectrosc. **41,** 1340 (1991).
27. O. Axner and S. Sjostrom, Appl. Spectrosc. **44,** 864 (1990).
28. J. C. Travis, J. Chem. Educ. **59,** 909 (1982).
29. O. Axner, M. Norberg, and H. Rubinsztein-Dunlop, Spectrochim. Acta **44B,** 693 (1989).
30. L. Volk, W. Richardson, K. H. Lau, M. Hall, and S. H. Lin, J. Chem. Educ. **54,** 95 (1977).
31. L. De Galan and G. F. Samaey, Spectrochim. Acta **25B,** 245 (1970).
32. R. F. Browner and J. D. Winefordner, Anal. Chem. **44,** 247 (1972).
33. G. F. Kirkbright, M. Sargent, and S. Vetler, Spectrochim. Acta **25B,** 465 (1970).
34. M. Omenetto, D. Benetti, and G. Rossi, Spectrochim. Acta **27B,** 453 (1972).
35. H. Haraguchi, B. Smith, S. Weeks, D. J. Johnson, and J. D. Winefordner, Appl. Spectrosc. **31,** 156 (1977).
36. H. Haraguchi and J. D. Winefordner, Appl. Spectrosc. **31,** 195 (1977).
37. J. Wang, S. Li, X. Wang, W. Li, Z. Chen, and Y. Luo, Spectrosc. Lett. **25,** 769 (1992).
38. M. A. Fernandez and G. J. Bastiaans, Appl. Spectrosc. **33,** 145 (1979).
39. G. F. Kirkbright, M. K. Peters, M. Sargent, and T. S. West, Talanta **15,** 663 (1968).
40. A. C. Eckbreth, in *Laser Probes for Combustion Chemistry,* D. R. Crosley, Ed. ACS Symp. Ser. No. 134 (American Chemical Society, Washington, D.C., 1980), pp. 271–301.
41. G. A. Petrucci, D. Imbroisi, B. W. Smith, and J. D. Winefordner, Spectrochim. Acta **49B,** 1569 (1994).
42. G. A. Petrucci, D. Imbroisi, R. D. Guenard, B. W. Smith, and J. D. Winefordner, Appl. Spectrosc. **49,** 655 (1995).
43. W. L. Wiese and G. A. Martin, *Wavelengths and Transition Probabilities for Atoms and Atom Ions,* Part II, NSRDS-NBS 68 (U.S. Government Printing Office, Washington, D.C., 1980).